

# Dark and Baryonic Matter in Bright Spiral Galaxies: II. Radial Distributions for 34 Galaxies

Susan A. Kassin<sup>1,2</sup>, Roelof S. de Jong<sup>3</sup>, & Benjamin J. Weiner<sup>4</sup>

## ABSTRACT

We decompose the rotation curves of 34 bright spiral galaxies into baryonic and dark matter components. Stellar mass profiles are created by applying color- $M/L$  relations to near-infrared and optical photometry. We find that the radial profile of the baryonic-to-dark-matter ratio is self-similar for all galaxies, when scaled to the radius where the contribution of the baryonic mass to the rotation curve equals that of the dark matter ( $R_X$ ). We argue that this is due to the quasi-exponential nature of disks and rotation curves that are nearly flat after an initial rise. The radius  $R_X$  is found to correlate most strongly with baryonic rotation speed, such that galaxies with  $R_X$  measurements that lie further out in their disks rotate faster. This quantity also correlates very strongly with stellar mass, Hubble type, and observed rotation speed;  $B$ -band central surface brightness is less related to  $R_X$  than these other galaxy properties. Most of the galaxies in our sample appear to be close to maximal disk. For these galaxies, we find that maximum observed rotation speeds are tightly correlated with maximum rotation speeds predicted from the baryon distributions, such that one can create a Tully-Fisher relation based on surface photometry and redshifts alone. Finally, we compare our data to the NFW parameterization for dark matter profiles with and without including adiabatic contraction as it is most commonly implemented. Fits are generally poor, and all but 2 galaxies are better fit if adiabatic contraction is not performed. In order to have better fits, and especially to accommodate adiabatic contraction, baryons would need to contribute very little to the total mass in the inner parts of galaxies, seemingly in contrast with other observational constraints.

*Subject headings:* galaxies: fundamental parameters – galaxies: general – galaxies: halos – galaxies: kinematics and dynamics – galaxies: spiral – galaxies: stellar content

---

<sup>1</sup>Department of Astronomy, The Ohio State University

<sup>2</sup>currently at: UCO/Lick Observatory, University of California, Santa Cruz, CA 95064; kassin@ucolick.org

<sup>3</sup>Space Telescope Science Institute, 3700 San Martin Drive, Baltimore, MD 21218

<sup>4</sup>Department of Astronomy, University of Maryland, College Park, MD 20742

## 1. Introduction

The flatness of rotation curves has long been the most direct evidence for the existence of a dominant component of dark matter in spiral galaxies (Sofue & Rubin 2001). However, the distribution of dark matter is poorly constrained, even in galaxies where the presence of dark matter is dominant (e.g., Ver-

heijen 1997; de Block & McGaugh 1998). Interestingly, the main uncertainty in the radial density distribution of dark matter, as derived from rotation curves, stems from the poorly known stellar mass distribution (e.g., Verheijen 1997).

In this paper, we do not rely on the typical maximal disk assumption (van Albada et al. 1985; van Albada & Sancisi 1986) to derive stellar mass profiles, but use color-mass-to-light ratio ( $M/L$ ) relations first given by Bell & de Jong (2001) and later updated by Bell et al. (2003). These color- $M/L$  relations were determined from the analysis of spectrophotometric spiral galaxy evolution models and give an upper limit to the baryonic mass present in spirals. They are most powerful when applied to data in the near-infrared since this wavelength regime traces the older stellar populations that contain most of the mass, while avoiding much of the effects of dust (extinction at the near-infrared  $K$ -band is only about 10% of that at the optical  $B$ -band; Martin & Whittet 1990). The color- $M/L$  relations allow us to investigate radial variation in stellar  $M/L$ , and provide us with a consistent way of scaling stellar  $M/L$  from one galaxy to the next. With the distributions of stellar mass in galaxies reasonably well determined, we can begin to investigate those of the dark matter.

The maximum disk assumption (Sackett 1997) can be examined with the color- $M/L$  relations. We can obtain an upper limit to the number of galaxies that have maximal disks, and also compare the shapes of rotation curves derived from baryonic mass distributions in galaxies to the observed rotation curves as in Palunas & Williams (2000). There are many pieces of evidence in the literature for maximal disks; we mention a few noteworthy ones here. Possibly the strongest evidence comes from the work of Weiner, Sellwood, & Williams (2001) who used fluid-

dynamical models of gas flow to model the two-dimensional velocity field of a barred galaxy. They find that such models require 80 – 100% of the maximal disk  $M/L_I$  value. Palunas & Williams (2000) modeled the baryonic mass distributions of 74 spirals and found that a mass-follows-light model could reproduce the overall structure of the optical rotation curves in the majority of galaxies. These authors found that 75% of the galaxies in their sample have a rotation curve out to  $R_{23.5}$  that is entirely accounted for by baryons. The mass models for 20% of their sample fail because of nonaxysymmetric structures. For a more inclusive discussion on maximal disks, see Palunas & Williams (2000).

It has been known for nearly 20 years that the radius where dark matter begins to contribute to the rotation curve of a galaxy is smaller for low surface brightness galaxies than it is for brighter galaxies (e.g., Persic & Salucci 1988, 1990; Broeils 1992; Persic, Salucci, & Stel 1996; de Blok & McGaugh 1997). A number of authors have demonstrated this by evaluating either the mass discrepancy of galaxy disks (ratio of total to baryonic mass) by adopting a stellar  $M/L$ , or a similar quantity at a chosen radius. For example, Persic, Salucci, & Stel (1996) find that spiral galaxies with  $V = 100 \text{ km s}^{-1}$  have  $> 75\%$  of their mass in dark matter within  $R_{opt} \equiv 3.2h$  where  $h$  is the disk scale-length, and that galaxies with  $V = 150 \text{ km/s}$  have only  $> 40\%$ . McGaugh & de Blok (1998) find that the total  $M/L_B$  evaluated at  $4h$  is smaller for galaxies of higher surface brightness and brighter magnitude, and does not correlate with  $h$ . These authors also find that the radius where dark matter begins to dominate over the luminous mass is greater for higher surface brightness galaxies. Zavala et al. (2003) find that the ratio of the velocity due to the baryons to the total maximum velocity depends mainly on disk central surface

density such that denser galaxies have larger ratios. These authors also find that the mass discrepancy evaluated at  $2.2h$  and  $5h$  depends on central surface brightness, but puzzlingly does not depend on  $h$ , baryonic mass, or  $B$ -band luminosity. In addition, Zavala et al. (2003) find that  $M/L_B$  anti-correlates significantly with  $B$ -band central surface brightness and does not correlate with  $B$ -band luminosity, in disagreement with McGaugh & de Blok (1998) and the general qualitative trend in the literature. Most recently, Pizagno et al. (2005) evaluate the total  $M/L_i$  at  $2.2h_i$  and find median values of 2.4 and 4.4 for galaxies with stellar masses greater than  $10^{10}M_\odot$  and 4.4 between  $10^9$ – $10^{10}M_\odot$ , respectively. These authors are all generally in qualitative agreement, but there are discrepancies, and we will discuss their origin in the body of this paper.

A combination of resolved  $H\alpha$  or CO and H I velocity data is necessary to determine the dark matter distribution of a galaxy from its center to beyond  $\sim 5h$ .  $H\alpha$  data are essential to measure the steep rise of rotation curves in the inner  $\sim 2h$  of galaxies (e.g., Palunas & Williams 2000), whereas H I data are key to probe beyond where  $H\alpha$  can be measured (e.g., de Blok & McGaugh 1997). Since rotation curves in the optical portion of galaxies are usually affected by non-axisymmetric structures that do not trace the main galactic potential, such as bars and spiral arms, the distributions of dark matter derived from  $H\alpha$  data can be quite variable. Two examples of studies probing dark matter distributions that have used both types of rotation curves in a direct manner, independent of prior parameterizations for the dark matter, are Persic, Salucci, & Stel (1996) and McGaugh & de Blok (1998). Persic, Salucci, & Stel (1996) coadd 1100 rotation curves and find that they could be determined by a single galactic parameter (e.g., luminosity). This formulation, however, is refuted by a number of authors

(e.g., Verheijen 1997; Bosma 1981). McGaugh & de Blok (1998) find a regularity between the mass discrepancy and acceleration of a galaxy as a function of radius. This follows directly from the Tully-Fisher relation, probably the best observational example of self-similarity in the dark matter component of galaxies. The mass discrepancy-acceleration relation shows that knowledge of the baryonic mass distribution of a galaxy allows one to calculate its dark matter distribution. Such a relation steps beyond the usual Tully-Fisher relation, which predicts the dark matter content of a galaxy at a particular radius given its baryonic mass at that radius, to one that predicts radial distributions.

Theories and simulations of galaxy formation should be able to reproduce the distributions of dark matter observed in galaxies. Until now, comparisons to predictions for dark matter distributions have consisted of fits of functional formulations for dark matter halos to rotation curve data, with stellar  $M/L$  as a free parameter. Now that we have a handle on the stellar  $M/L$  in galaxies with the color- $M/L$  relations, we re-examine these fits. In particular, we test the main incarnation of the density distribution of dark matter halos in N-body simulations of a  $\Lambda$ CDM universe: the formulation of Navarro, Frenk, & White (1996) (NFW), which is the simplest and most popular analytical description. This formulation predicts that dark matter is significant down to the very inner radii of galaxies, in contradiction to maximal disks. Moreover, dark matter halos are expected to contract due to baryon collapse. As this contraction is normally implemented (Blumenthal et al. 1986), even more dark matter is caused to move toward the centers of galaxies, making the situation worse (e.g., McGaugh & de Blok 1998). We perform fits to the NFW formulation with and without including contraction as it is normally implemented. The main as-

sumption behind these fits, namely that the NFW halos can be fit to data that subtends only their very inner parts ( $\lesssim 0.1R_{\text{virial}}$ ), is problematic. Furthermore, the simulations that produce the NFW functions have difficulty forming disk galaxies once hydrodynamics is included (e.g., Abadi et al. 2003), signaling possible unknown interactions between baryons and dark matter. To address these concerns, we turn the problem of fitting dark matter halos to data around and present a simple universal form for dark matter profiles in terms of baryonic mass profiles.

This paper is organized as follows: In §2 we briefly discuss our galaxy sample. Radial baryonic mass distributions and their rotation curves are derived in §3. In §4 these baryonic rotation curves are compared with rotation curves from the literature to derive rotation curves due to dark matter. We discuss maximal disks in §5. In §6 we define quantities to describe the baryonic and dark matter distributions and show how they correlate with general galaxy properties. We investigate the radial behavior of dark matter in §7, and mass profiles are fit with the NFW profile in §8. In §9, we summarize our conclusions. Throughout this paper we adopt a Hubble constant ( $H_o$ ) of  $70 \text{ km s}^{-1} \text{ Mpc}^{-1}$ . When distance-dependent quantities have been derived from the literature, we have reduced them to this value of  $H_o$  and always quote the converted values.

## 2. The Galaxy Sample

Our data consist of surface brightness profiles, physical parameters, and rotation curves for 34 bright spiral galaxies. These galaxies have inclinations in the range  $\sim 30$ – $65$  degrees in order to reduce the effects of dust, while still being able to obtain accurate kinematical information. Surface brightness profiles for 30 galaxies were presented in Kassin, de Jong, & Pogge (2005) (hereafter, Paper I); those for

the remaining 4 galaxies can be found in Verheijen (1997). More details on the sample selection are given in Paper I. The profiles were calculated in elliptical annuli of increasing distance from the centers of the galaxies and have been corrected for Galactic extinction. The galaxies NGC 1090, NGC 2841, and NGC 3198, which have images from the Sloan Digital Sky Survey (SDSS) Second Data Release (Abazajian et al. 2004), have images in which almost half of the galaxy was off of the detector. This is also the case, but to a much lesser extent for NGC 3521. This effect can be observed in the  $g$ -band images in Figure 1 of Paper I; these galaxies are flagged in the following analysis. All the analyses in this paper have been performed for both the approaching and receding sides of a handful of galaxies with complete imaging. No significant change (to within the zero-point uncertainties) was found between the results for each side of these galaxies. Physical parameters (i.e., Hubble type, distance,  $R_{25}$ , integrated magnitudes) and bulge-disk decompositions can also be found in Paper I.

## 3. Baryonic Matter

In this section, we derive the baryonic mass surface density profiles of the galaxies, and compute the component of the galaxies’ observed rotation that is due to the baryons. These components are called “baryonic rotation curves,” to distinguish them from observed rotation curves. In §4, we will introduce the term “dark matter rotation curves,” to denote the contribution from dark matter to the observed rotation curves.

### 3.1. Radial Baryonic Surface Mass-Density Distributions

To determine a galaxy’s radial stellar surface mass-density distribution, we apply a color- $M/L$  relation to its surface brightness

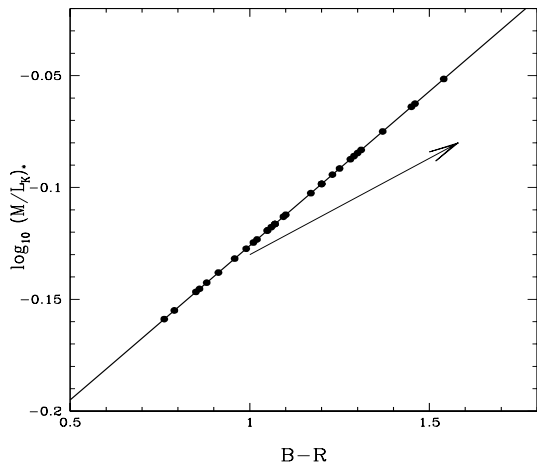


Fig. 1.— Color- $M/L$  relation for  $B-R$  color and  $(M/L)_*$  at  $K$  from Bell et al. (2003) (solid line). The galaxies in the sample are plotted as filled circles, and a reddening vector is plotted for correction to face-on for a Milky Way-type galaxy viewed at an inclination of  $80^\circ$  with the Tully et al. 1998 formalism.

profiles. These relations were derived from spectrophotometric spiral galaxy evolution models in Bell & de Jong (2001), and were updated in Bell et al. (2003). The color- $M/L$  relations show a relatively tight correlation ( $\sim 0.1$  dex spread for the color and metallicity range where our galaxies lie) between the optical color of a galaxy and its stellar mass-to-light ratio,  $(M/L)_*$ . Color- $M/L$  relations are most useful when applied to  $(M/L)_*$  in the near-infrared since they are the least affected by dust obscuration, as discussed in Bell & de Jong (2001). Specifically, we choose to use the relation between  $B-R$  color and  $(M/L)_*$  in the  $K$ -band. This relation is composed of the optical color with the largest wavelength baseline and the reddest near-infrared band. It is reproduced in Figure 1. If imaging is unavailable at  $R$ , we use the relation for  $B-V$ , and if imaging is unavailable at  $K$  we use  $H$ .

For those galaxies without a significant

bulge contribution (such that inclusion of a bulge component does not change the rotation curve due to baryons beyond the uncertainties of the color- $M/L$  relations), we apply a color- $M/L$  relation directly to the azimuthally averaged radial  $B-R$  color profiles to derive radial  $(M/L)_*$  profiles at  $K$ . The  $L_K$  profile for each galaxy is then multiplied by the galaxy’s  $(M/L)_*$  profile to derive a radial stellar surface mass-density profile. For these galaxies, using a radial  $B-R$  color profile is consistent with using an aperture  $B-R$  color since this color- $M/L$  relation has a shallow slope. For those galaxies with a significant bulge component, a bulge-disk decomposition is performed. A characteristic  $B-R$  color is adopted for each component based on the average colors of the bulge and disk, and the  $L_K$  profiles are multiplied by the resulting  $(M/L)_*$ . Extinction corrections are discussed in §3.4. We also extend the exponential disk surface brightness profiles until approximately  $\infty$  (defined here as  $r = 10000''$ ).<sup>1</sup>

When available from the literature, we use radial H I 21 cm measurements to determine the contribution of interstellar gas to the radial baryonic surface mass-densities. There are gas measurements available for NGC 1090 from Gentile et al. (2004), NGC 3198 from Begeman (1987), and NGC 3949, NGC 3953, and NGC 3992 from Verheijen (1997). The neutral gas component is included by scaling the H I surface mass-density by a factor of 1.32 to account for the abundance of helium. For those galaxies without gas mass measurements, we assume that gas does not contribute to its baryonic surface mass-density. This is probably not a bad assumption for high surface brightness galaxies since a galaxy with a Hubble type between Sa and Scd has a gas mass fraction that is typically

<sup>1</sup>Extended galactic stellar disks have been discovered for some galaxies via very deep imaging (see Ibata et al. 2005, and references within).

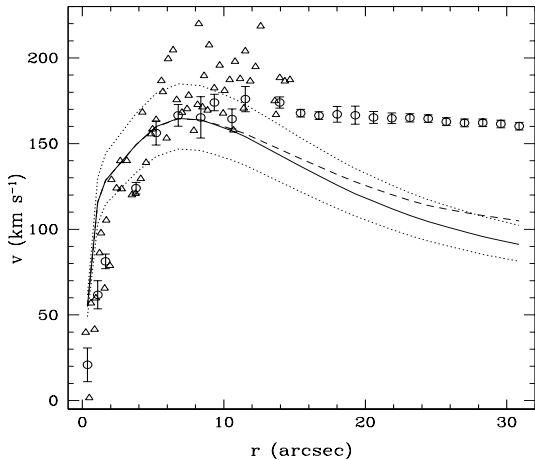


Fig. 2.— Rotation curve for NGC 1090 due to the stellar mass component (solid line) is compared with the rotation curve due to stars and H I gas from Gentile et al. 2004 (dashed line). The observed H $\alpha$  and H I rotation curves are plotted as open triangles and circles, respectively. The upper and lower bounds for the stellar mass rotation curve (dotted lines) are due to the 0.1 dex uncertainty in the color- $M/L$  relations.

$M_{HI}/M_{gas+stars} \approx 0.03$  (Roberts & Haynes 1994), and hence does not greatly affect its baryonic mass. The average gas mass fraction for the 5 galaxies in our sample that have gas mass measurements is 0.04, consistent with this measurement. Figure 2 demonstrates the effect of including the interstellar gas component in the baryonic rotation curve of NGC 1090, which is generally within the uncertainty of the stellar mass rotation curve. Therefore, by not including interstellar medium contributions in the analysis, only a minor systematic effect is introduced.

### 3.2. Baryonic Rotation Curves

A baryonic rotation curve is calculated for each galaxy from its baryonic surface mass-density profile and is plotted in Figure 3. The rotation curve calculation is done with the

rotmod task in the GIPSY software package (van der Hulst et al. 1992), which calculates rotation curves for galaxies composed of a truncated exponential disk (Casertano 1983) and a spherical bulge when applicable. Exponential disks are assumed to have a scale-height of 0.3 kpc, which is typical of bright spirals. The difference between using a different scale-height for each galaxy of  $0.1h_{IR}$  kpc, as in Sparke & Gallagher (2000), and a global value of 0.3 kpc is negligible. The results also remain unchanged if we used the relation between the central surface brightness and the ratio of vertical scale-height to vertical scale-length given by Bizyaev & Mitronova (2002).

### 3.3. Uncertainties in Baryonic Rotation Curves

The largest source of uncertainty for the baryonic rotation curves lies in the normalization of the color- $M/L$  relation, which is mainly determined by the stellar IMF at low-mass. Since the faint end of the IMF is relatively unconstrained, there may exist many low-mass, low-luminosity stars that can contribute significantly to the mass budget of a stellar population without creating a detectable increase in luminosity or change in color. For their derivation of the color- $M/L$  relations, Bell & de Jong (2001) and Bell et al. (2003) adopted a truncated Salpeter IMF which derives from the constraint that baryonic rotation curves should not over-predict observed rotation curves for spiral galaxies in Ursa Major (the Verheijen 1997 sample). With this constraint, they predict fewer low mass stars than a Salpeter IMF. These relations thus give an *upper limit* to the stellar mass present; a lower normalization of the color- $M/L$  relation cannot be excluded.

We re-derive this constraint on the upper limit to the IMF by re-calculating maximum disk fits for galaxies in the Verheijen (1997) sample without including a dark halo, as was

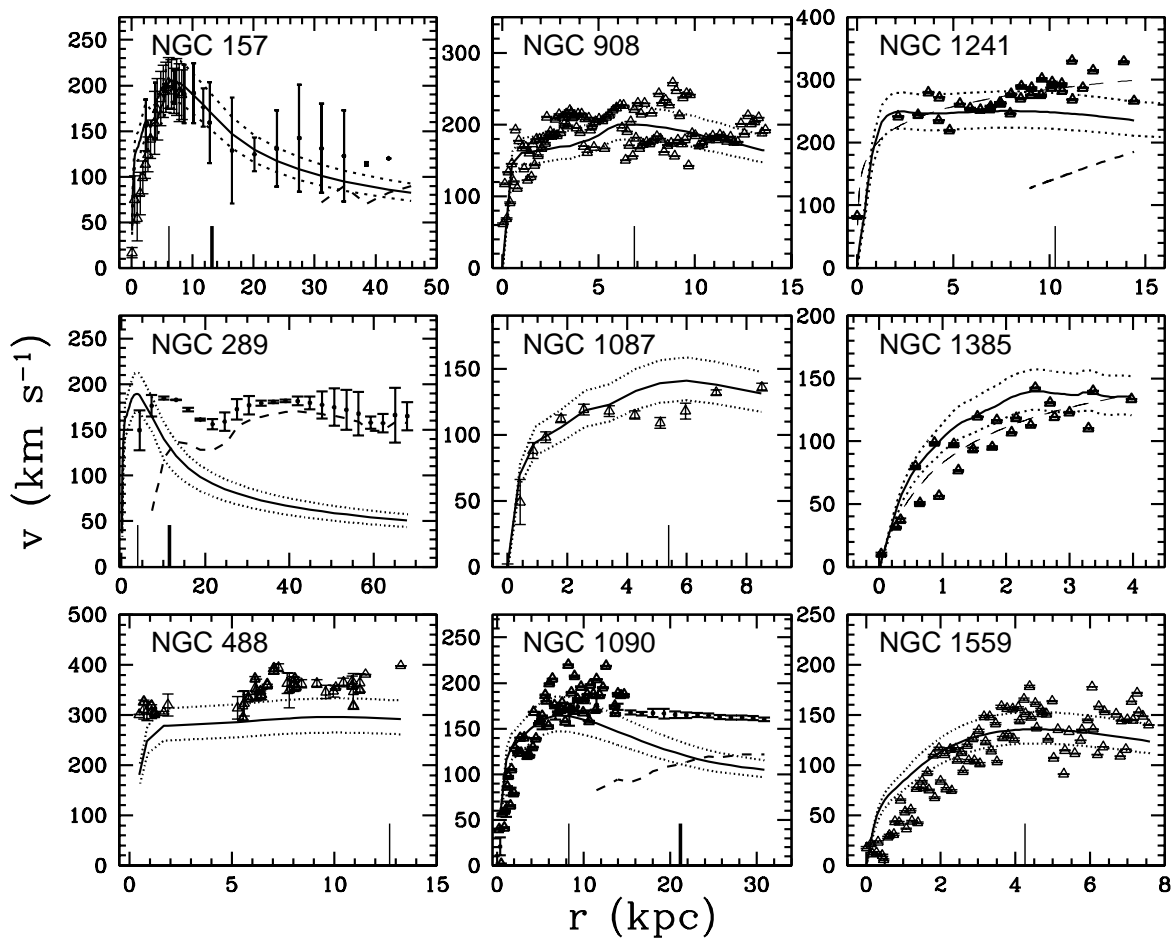


Fig. 3a.— Observed rotation curves (dots for H I, triangles for H $\alpha$  or N II, thin dashed lines for models), baryonic rotation curves (solid lines), and dark matter rotation curves where applicable (thick dashed lines). For many of the H $\alpha$  and N II rotation curves, the error bars are smaller than the points at the resolution of the plots. The effects of the  $\pm 0.1$  dex uncertainty in the color- $M/L$  relations on the baryonic rotation curves are plotted as dotted lines. On the x-axis, the radii  $R_{25}$  and  $R = 2.2h_{IR}$  are marked with thick and thin bars, respectively.

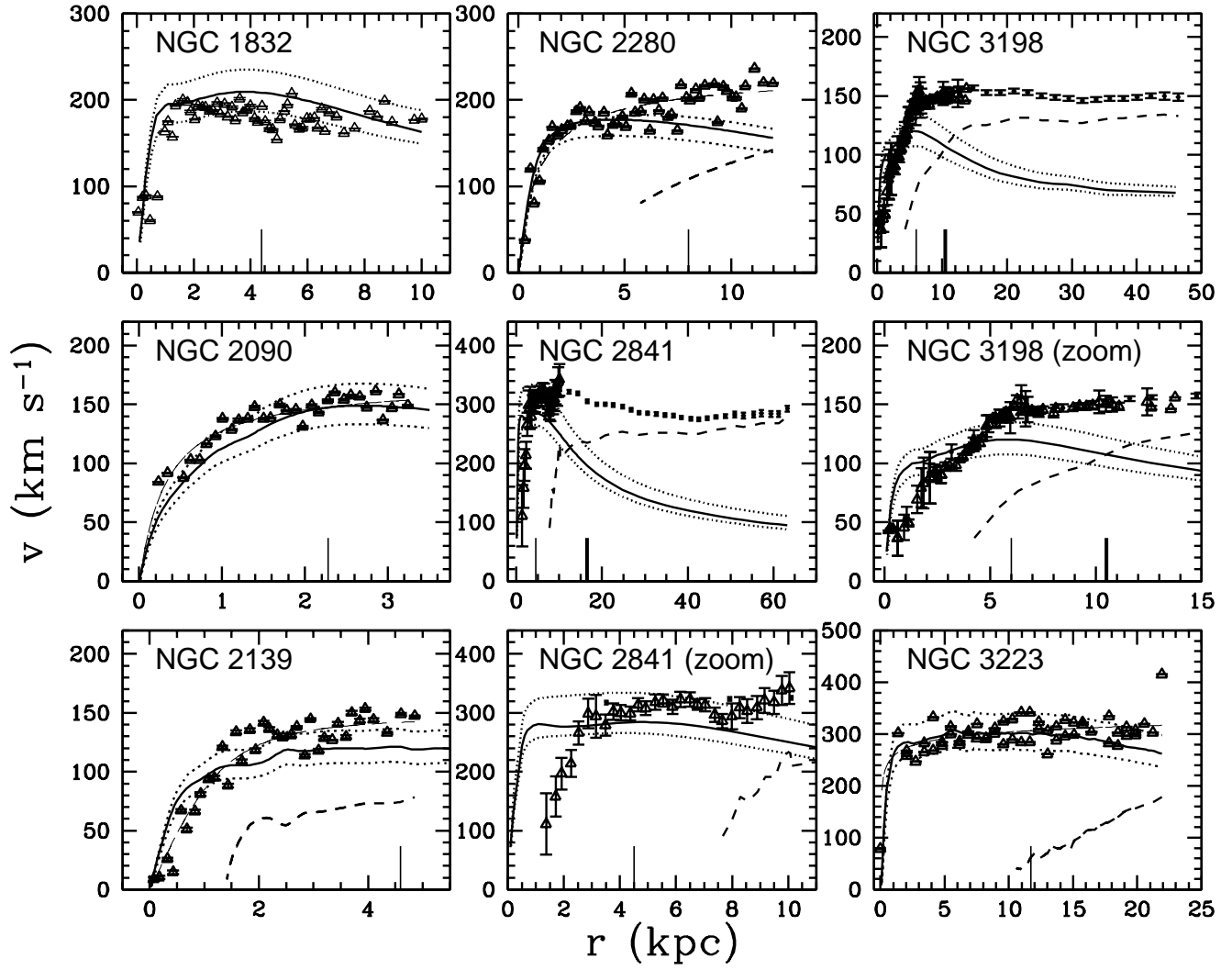


Fig. 3b.— See Figure 3a.



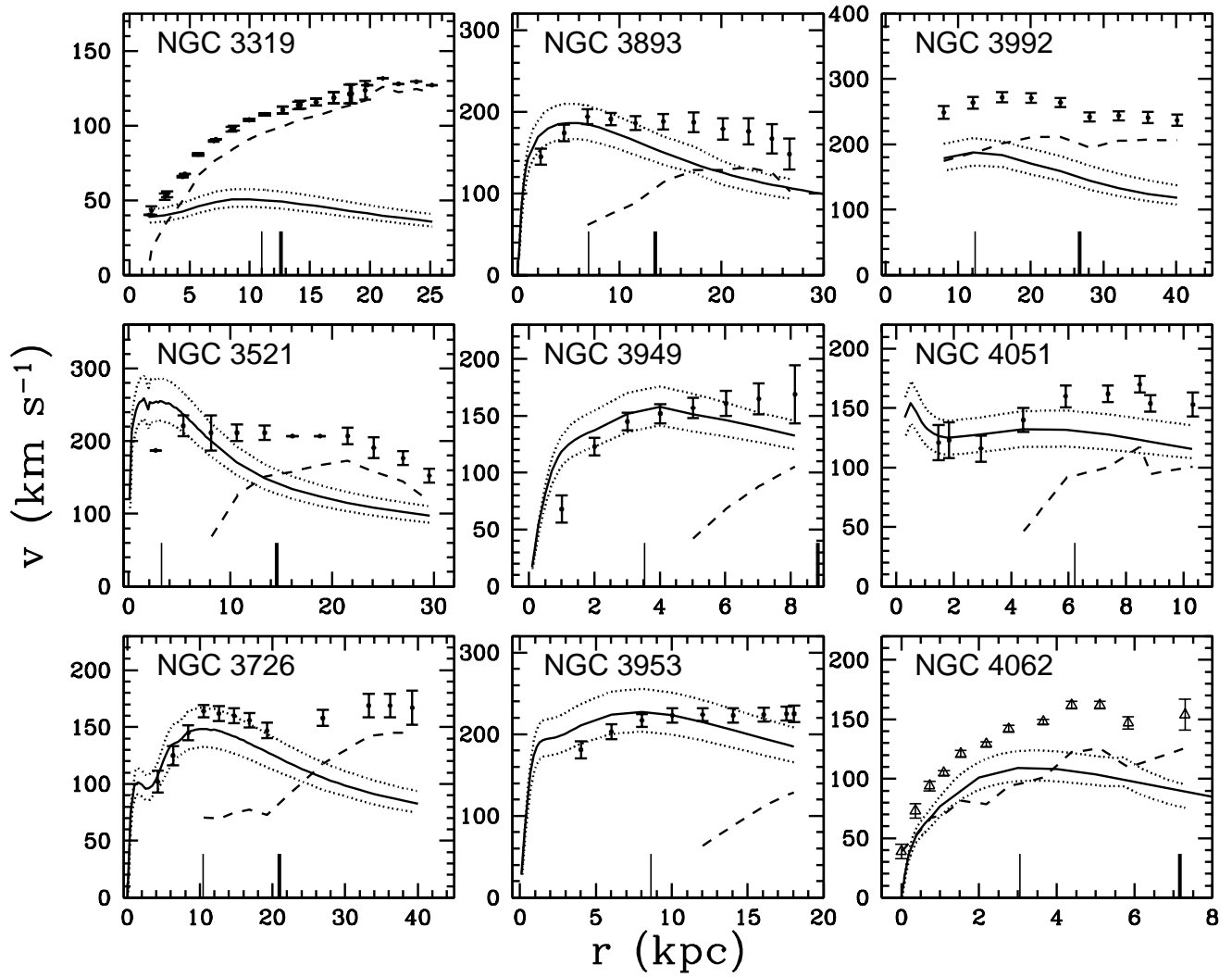


Fig. 3c.— See Figure 3a.

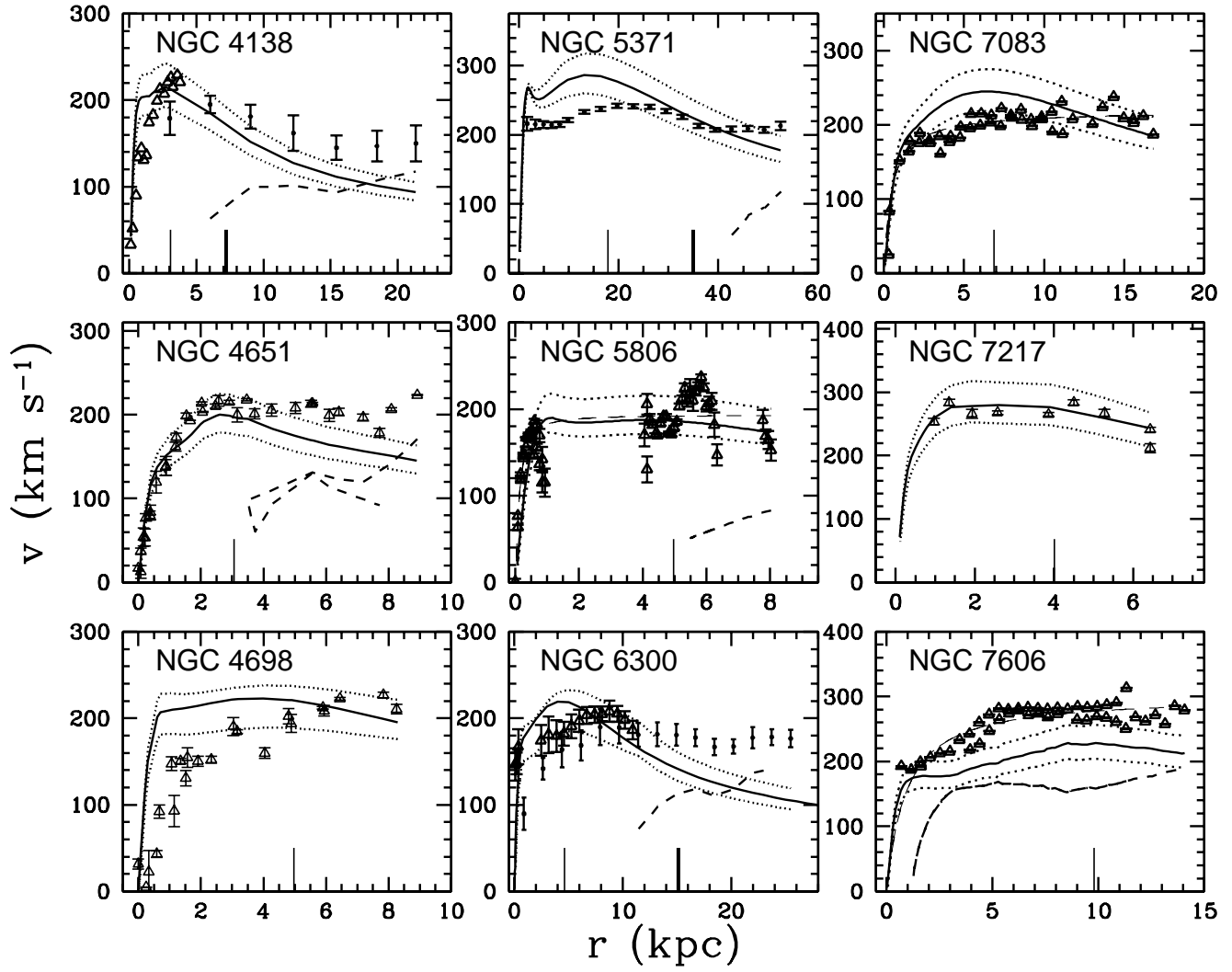


Fig. 3d.— See Figure 3a.

done in the original Verheijen (1997) fits. For these fits, we define maximal disk to be the greatest possible contribution of the bulge and disk to the observed rotation curve of the galaxy. To do this, we scale the  $K$ -band derived stellar mass rotation curves as high as possible without over-predicting the observed rotation curves beyond the very inner parts. In order to best match the overall shapes of the observed rotation curves, we allow over-predictions of the inner 2 points of H I rotation curves due to beam-smearing and over-predictions of the inner parts of H $\alpha$  rotation curves. We also re-scale the stellar and gas mass distributions from the distance used in Verheijen (1997) to 20.7 Mpc before fitting the maximal disks, unlike the approximate re-scaling done in Bell & de Jong (2001). Gas distributions derived from H I measurements are multiplied by 1.32 to account for helium, as in Verheijen (1997). In Figure 4, the resulting maximum disk  $(M/L)_*$  are plotted against the  $B - R$  colors of the galaxies corrected for extinction with the Tully et al. (1998) formalism. In this figure, we also plot maximum disk  $(M/L)_*$  for those galaxies presented in this paper that have  $BRK$  photometry. All the points in Figure 4 are upper limits to the  $(M/L)_*$ ; galaxies cannot have values greater than those defined by the lower envelope in this plot without over-predicting their rotation curves beyond the very inner parts. It is apparent from Figure 4 that the Bell et al. (2003) color- $M/L$  relation is consistent with all the galaxies to within  $\sim 0.1$  dex, which is the uncertainty in the relations.

Other than the IMF, there are five primary sources of uncertainty in the determination of the baryonic surface mass-density distributions: uncertainties in the distances to galaxies<sup>2</sup>, 0.1 dex spread in the color- $M/L$

<sup>2</sup>Of the 34 galaxies in our sample, 4 have distances estimated from Cepheid variables for which the uncertainties are much less than other types of distance

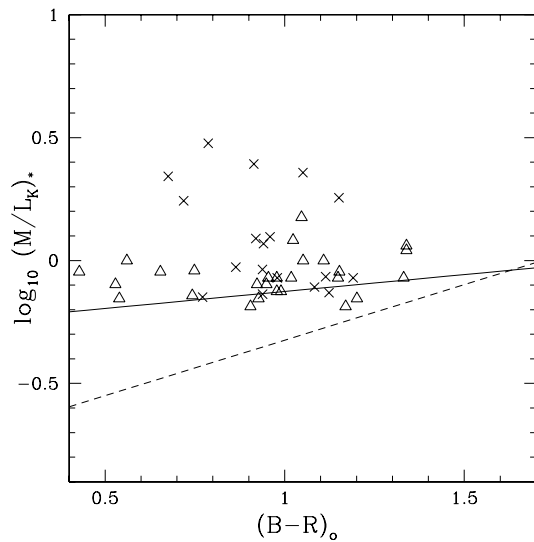


Fig. 4.— Maximum disk stellar  $(M/L_K)_*$  versus reddening-corrected  $B - R$  colors for galaxies in the Verheijen (1997) sample (Xs) and in this paper (triangles). Plotted for reference are the color- $M/L$  relations of Bell & de Jong 2001 (dashed line) and Bell et al. 2003 (solid line).

relations, uncertainties in the zero-points of these relations, uncertainties in the photometric zero-point calibrations, and uncertainties in the determination of a galaxy’s inclination to the line of sight. Secondary sources of uncertainty generally have a small effect on the baryonic rotation curves. They include secondary photometric (“bootstrap”) calibrations, the neglect of interstellar gas content, and position angle uncertainties. Dust reddening also plays a role in the uncertainty of the baryonic rotation curves; this will be discussed in §4.3. Note that the transformation of Two Micron All Sky Survey (2MASS; Jarrett et al. 2000; Cutrie et al. 2000; Jarrett et al. 2003) and SDSS photometry to the Kron-Cousins system introduces negligible uncertainties, as shown in Paper I.

As an illustration, Figure 5a–d shows the measurements, and are typically  $\sim 10\%$ .

effects of three of the primary sources of uncertainty on the baryonic rotation curve of NGC 157. In all the plots in Figure 5, we plot  $|\Delta v_b|/v_b$  where  $\Delta v_b$  is the difference between the velocity derived from the color- $M/L$  relations and this velocity affected by the named uncertainty. Figure 5a shows the effect of an uncertainty of  $\pm 20\%$  in the distance. The distance uncertainty causes a maximum change in  $|\Delta v_b|/v_b$  of 0.24 which corresponds to a change in the velocity of nearly 40 km s<sup>-1</sup>. The average change is  $|\Delta v_b|/v_b = 0.09$  ( $|\Delta v_b| \simeq 13$  km s<sup>-1</sup>). Figure 5b shows the effect of a systematic change of  $\pm 0.1$  dex in the color- $M/L$  relations. This uncertainty causes a maximum change in  $|\Delta v_b|/v_b$  of 0.12 ( $|\Delta v_b| \simeq 25$  km s<sup>-1</sup>), and an average change of 0.12 ( $|\Delta v_b| \simeq 20$  km s<sup>-1</sup>). In Figure 5c,d, the effects of introducing systematic errors in the photometric zero-point calibrations are shown. In Figure 5c, the effect of the actual zero-point uncertainties for NGC 157 is shown ( $\sigma_B = 0.03, \sigma_R = 0.03, \sigma_K = 0.04$ ). This causes an average change in  $|\Delta v_b|/v_b$  of 0.10 ( $|\Delta v_b| \simeq 17$  km s<sup>-1</sup>). While most of our optical photometric zero-points are good to  $\leq 5\%$ , the worst uncertainty in an optical zero-point calibration for any of the surface brightness profiles that we use in this analysis is  $\pm 15\%$ , as given in Table 3 of Paper I. All of the uncertainties on the near-infrared zero-points are  $\sim 4\%$ . To show the effect of a photometric calibration that is not as good as that of NGC 157, in Figure 5d we show what would happen to the rotation curve if photometric zero-point errors were  $\pm 15\%$  in the optical and  $\pm 4\%$  in the near-infrared. Such uncertainties cause an average change in  $|\Delta v_b|/v_b$  of 0.13 ( $|\Delta v_b| \simeq 22$  km s<sup>-1</sup>).

In Figure 5e,f, we show the effects on the baryonic rotation curve of NGC 157 of changing the inclination and position angle in the derivation of its surface brightness profiles. Typical uncertainties in position angles and

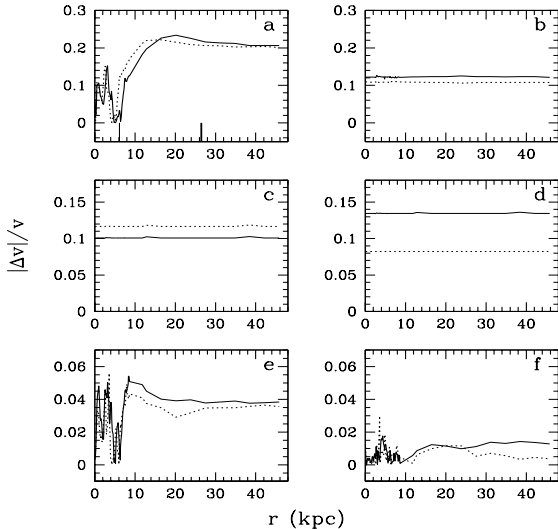


Fig. 5.— Effects of uncertainties on the baryonic rotation curve of NGC 157. For one side of the uncertainty (e.g., +0.1 dex), the  $|\Delta v_b|/v_b$  curve is plotted as a dotted line, and for the other side (e.g., -0.1 dex) the curve is plotted as a solid line. The effects of the following uncertainties are plotted: (a)  $\pm 20\%$  uncertainty in the distance to the galaxy, (b)  $\pm 0.1$  dex scatter in the color- $M/L$  relation, (c) actual photometric zero-point uncertainties for NGC 157, (d) photometric zero-point uncertainties for the galaxy with the poorest zero-point, (e) a change in the inclination of  $5^\circ$ , and (f) a change in the position angle of  $5^\circ$ . The radii  $2.2h_K$  and  $R_{25}$  are marked as thin and thick lines, respectively, on the x-axis in panel a.

inclinations are both  $\sim \pm 5^\circ$  (Paper I). In Figure 5e, we plot the effect of a change in the position angle of  $\pm 5^\circ$ , and in Figure 5f we show the effect of a change in the inclination of  $\pm 5^\circ$ . Uncertainties in the inclination have a larger effect (on average  $|\Delta v_b| \simeq 0.03$ ;  $|\Delta v_b| \simeq 5$  km s<sup>-1</sup>) than those in the position angle (on average  $|\Delta v_b| \simeq 0.007$ ;  $|\Delta v_b| \simeq 1$  km s<sup>-1</sup>). However, both these uncertainties are small when compared to other sources of error discussed in this section.

In Figure 6, to compare the color- $M/L$  re-

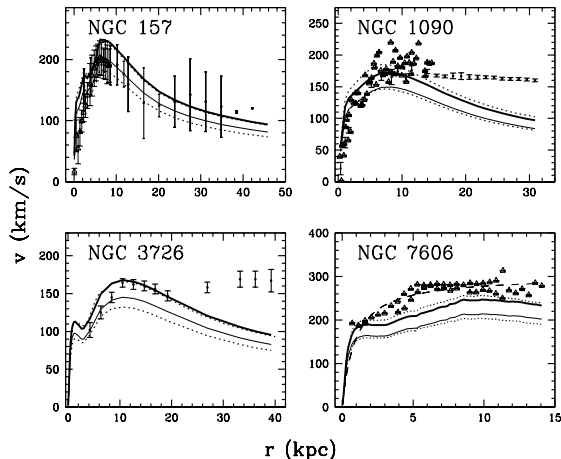


Fig. 6.— Baryonic rotation curves derived from the color- $M/L$  relations (plotted as dotted lines for the  $\pm 0.1$  dex scatter in the relations) are compared with baryonic rotation curves derived from constant  $(M/L_K)_*$  of 0.75 (thin solid line) and 1.0 (thick solid line). The thin dashed line plotted for NGC 7606 is the model observed rotation curve of Courteau 1997. All other features of the plot are the same as Figure 3.

lations to constant  $(M/L_K)_*$ , baryonic rotation curves created with the color- $M/L$  relations and with  $(M/L_K)_*$  of 0.75 and 1.0 are plotted for 4 example galaxies. The rotation curves created with  $(M/L_K)_*$  of 0.75 and 1.0 are approximately consistent with the  $\pm 0.1$  dex uncertainty of the color- $M/L$  relations. This is similarly the case for all galaxies in our sample, and is due to the shallow slopes of the color- $M/L$  relations ( $\sim 0.14$ – $0.18$  in  $\log_{10} M/L$ ).

To summarize, other than the IMF, of the other sources of uncertainty in the determination of the baryonic rotation curves, only the distance uncertainty, the  $\pm 0.1$  dex scatter in the color- $M/L$  relations, and zero-point uncertainties can produce non-negligible effects. These three sources of uncertainty vary from galaxy to galaxy and introduce scatter in the

baryonic rotation curves.

### 3.4. Effects Due to Dust

Since the reddening vector in Figure 1 lies nearly parallel to the color- $M/L$  relation, to first order, errors in foreground dust reddening estimates should not strongly affect the final relative derived masses of the stellar populations, as foreground dust will systematically both redden and extinguish galactic light. In this section, we discuss the possible effects of dust reddening and extinction on absolute derived stellar masses.

We examine the empirical inclination-dependent extinction correction of Tully et al. (1998), which should describe to first order the dust content of galaxies. We correct to face-on the total integrated colors and magnitudes of galaxies in our sample. In doing this, we ignore radial dust gradients in the disk and the fact that dust reddening is likely to be large for the inner parts of galaxies. While the  $K$ -band magnitudes barely change when extinction corrected (0.05 mag on average), the  $B - R$  colors do (0.09 mag on average). This, however, should not affect the final derived stellar masses, since the color- $M/L$  relations that we use have a very shallow slope in  $B - R$  color. To examine this effect further, for 4 galaxies that span the range of inclinations in our sample, we apply the Tully et al. (1998) extinction correction to their radial  $K$ -band profiles, and use their extinction-corrected  $B - R$  colors to derive  $(M/L_K)_*$ . From the resulting surface mass-density profiles, we derive baryonic mass rotation curves. In Figure 7, we plot for the 4 galaxies the difference between the extinction-corrected baryonic rotation curve and the uncorrected one. For NGC 157, NGC 3726, NGC 7217, and NGC 7606, the rotation curves on average differ by 1.3, 1.1, 2.7, and 5.0  $\text{km s}^{-1}$ , respectively. The greatest difference is for NGC 7606 which has the largest inclination

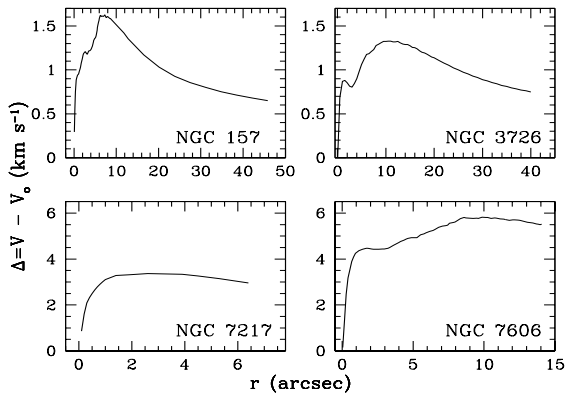


Fig. 7.— Difference between the extinction-corrected ( $V$ ) and uncorrected ( $V_o$ ) baryonic rotation curves. The extinction-corrected baryonic rotation curves are derived from colors and magnitudes corrected for extinction with the formalism of Tully et al. 1998.

of the four galaxies,  $63.9^\circ$ . These differences in velocity are all less than the uncertainties of the baryonic rotation curves themselves, as discussed in §3.3.

Galaxy disks have been observed to have a relatively constant face-on dust opacity of  $\sim 0.5$  magnitude in the  $I$ -band (Holwerda et al. 2005). Correcting for this,  $A_I$  would increase the baryonic velocity by  $\sim 20$   $\text{km s}^{-1}$ . However, since the maximal disk limits in Figure 4 would also need to be corrected, and the color- $M/L$  relations re-scaled accordingly, the net effect would more or less cancel out. However, it is very likely that more complex dust models where the effects of dust depend on star/dust geometry are necessary, such as those by Disney (1989) and Gordon et al. (2001). We choose to leave this approach to a future analysis, since the detailed radiative transfer codes are not publicly available and are difficult to apply to real galaxies. Moreover, different galaxies may have various amounts of dust and different star/dust geometries which would cause dust to affect

the baryonic rotation curve of each galaxy uniquely.

## 4. Dark Matter

For each galaxy, we compare its baryonic rotation curve derived in §3.2 with its observed rotation curve taken from the literature to derive a “dark matter rotation curve.”

### 4.1. Observed Rotation Curves

Observed rotation curves are plotted in Figure 3; Table 1 lists the tracer and literature reference for each. Some galaxies have two observed rotation curves, one from  $\text{H}\alpha$  or  $\text{N II}$  observations which traces the inner parts, and another from  $\text{H I}$  observations which traces the outer parts. If errors for the observed rotation curves were given in the original table or plot that they were taken from, then these are used in this paper. If no errors are given, then we estimate them to be the difference in rotation velocity between the approaching and receding sides of the galaxy; rotation curves for which we estimate the errors in this manner are noted in Table 1. This estimate will generally give errors larger than the true measurement errors since it will be more affected by non-axisymmetric features such as spiral arms and slight warps in the gas distributions. Note that the 2–3 innermost points of the  $\text{H I}$  rotation curves and the outer few points of the  $\text{H}\alpha$  and  $\text{N II}$  rotation curves have a greater uncertainty than other points due to beam smearing and low signal-to-noise, respectively. For many of the rotation curves we have obtained data from the authors, but for a handful we could not. For those few galaxies, rotation curves are extracted from plots in the literature with the DataThief program (Tummers 2000); these galaxies are noted in Table 1. Errors inherent to the extraction of a rotation curve vary from plot to plot, but tend to be  $\leq 5$   $\text{km s}^{-1}$ .

Galaxies marked with the reference “Mathewson & Courteau” in Table 1 are rotation curves that were originally presented in Mathewson, Ford, & Buchhorn (1992) and were later modeled by Courteau (1997). For these galaxies, we plot both the actual and model rotation curves in Figure 3. Since we are primarily interested in large-scale trends, we adopt the model rotation curves in the following analysis in order to avoid much of the fine structure inherent to the actual data.

#### 4.2. Dark Matter Rotation Curves

At those radii where the observed rotation speed of a galaxy is greater than that of its baryons, the additional gravitational component is assumed to be due to dark matter. A dark matter rotation curve is derived as the square root of the difference of the squares of the observed rotation velocity and the baryonic rotation curve velocity at each radius (Binney & Tremaine 1987). In doing this, it is assumed that the halos of galaxies are axially symmetric, the disk and halo are aligned, and the observed gas is in circular orbits. Dark matter rotation curves for the galaxies are plotted in Figure 3.

For 10 galaxies, the baryonic rotation curves over-predict the observed rotation curves for some range in radius<sup>3</sup>. These galaxies are NGC 157, NGC 1559, NGC 2139, NGC 2841, NGC 3198, NGC 4138, NGC 4698, NGC 5371, NGC 6300, and NGC 7083. The baryonic rotation curve for the -0.1 dex scatter in the color- $M/L$  relations also over-predicts for the first six galaxies listed above. However, for these six galaxies, the over-prediction oc-

<sup>3</sup>We do not include in this count baryonic rotation curves that over-predict the inner parts of H I rotation curves, since they are affected by beam-smearing in this region. Also, Figure 4 suggests that this number is less than 10, but we ignore the very inner parts of the galaxies when calculating maximal  $(M/L_K)_{*s}$  in §3.1.

curs only in the very inner parts where the observed rotation curve is affected by structures such as rings, bars, inner windings of spiral arms, and/or irregular morphology. Baryonic rotation curves are derived under the assumption of circular motion and need not trace such structures. For NGC 6300 and NGC 7083, the baryonic rotation curves for -0.1 dex do not over-predict the observed rotation curves. The galaxy NGC 6300 has a bar and a ring in the region where the over-prediction occurs, but the image of NGC 7083 shows no sign that its baryonic rotation curve should over-predict. This is somewhat acceptable, though, since the baryonic rotation curve for NGC 7083 for -0.1 dex does not over-predict.

Two galaxies, NGC 4698 and NGC 5371, have baryonic rotation curves that over-predict their observed rotation curves, even for the -0.1 dex scatter in the color- $M/L$  relations. For both these galaxies, the over-prediction cannot only be explained by bars and/or rings in the galaxy images. To examine things further, we create baryonic rotation curves using the position angle and inclination that were used to derive their observed rotation curves; the resulting curves also over-predict. Next, we create baryonic rotation curves for the -20% uncertainty in the galaxies’ distances and both the distance and color- $M/L$  uncertainties; they are plotted in Figure 8. For NGC 4698, the baryonic rotation curve created by taking into account both these effects still over-predicts. However, for this galaxy, its distance was calculated with a Virgo-centric infall calculation and was found to be triple-valued (Paper I). We derive a baryonic rotation curve for it with the distance solution which is closer than the one chosen in Paper I (9.7 Mpc, as opposed to the chosen solution of 19.1 Mpc). This baryonic rotation curve is plotted in Figure 8 and over-predicts only the inner portion ( $\sim 1.5$  kpc) of the observed rotation curve. For NGC 5371,

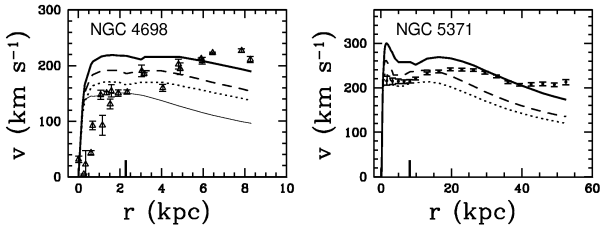


Fig. 8.— Effects on the baryonic rotation curves of the  $-0.1$  dex scatter in the color- $M/L$  relations and the  $-20\%$  uncertainty in distance for galaxies where the baryons over-predict the observed rotation curve. Original baryonic rotation curves (thick solid lines), those derived by taking into account the distance uncertainty (dashed lines), and those derived by taking into account both the distance uncertainty and the color- $M/L$  scatter (dotted lines) are triangles for  $H\alpha$  and small points for  $H I$ . For NGC 4698, we also plot the baryonic rotation curve derived from the adoption of a different distance to the galaxy (thin solid line). Observed rotation curves are plotted as points. The radius  $2.2h_{IR}$  is marked as a thick solid line on the x-axis.

the baryonic rotation curve created by taking into account the distance uncertainty over-predicts, while that created by taking into account both distance and color- $M/L$  uncertainties does not. The sort of over-prediction that is observed for NGC 4698 and NGC 5371 can also be due to such factors as a mis-measurement of the observed rotation curves and/or the effects of dust. A stellar population affected by dust may appear redder (and hence heavier and have a faster rotation) than it is intrinsically since the reddening effect of dust is slightly greater than its extinction effect. These galaxies could also signal a need to lower the normalization of the color- $M/L$  relations. If we did this, then many of the other galaxies in the sample would be sub-maximal, but the qualitative results of this paper would not change.

### 4.3. Uncertainties in Dark Matter Rotation Curves

Uncertainties in the dark matter rotation curves arise from a number of effects. The most significant are those inherent to the determination of the baryonic mass component, as discussed in §3.3. Other uncertainties include: non-circular motions that perturb the underlying potential (i.e., spiral arms, bars, substructure), statistical errors from the measurement of velocities in radial bins, systematic errors in measuring the velocity (i.e., beam smearing and slit position angle error), and uncertainties in the measurement of the dynamical centers of the galaxies. There also may be differences between the centers of galaxies determined from photometry and those determined from the observed rotation curves. However, center measurements are not expected to differ much since photometric centers are always chosen to be the brightest pixel in the nucleus which coincides with the dynamical center of most galaxies.

## 5. Maximal Disks

The radius  $R = 2.2h$  is where the rotation curve of a self-gravitating exponential disk reaches its peak (Freeman 1970). A commonly used definition of a maximal disk is given by Sackett (1997) where the galaxy *disk* provides  $85\% \pm 10\%$  of the total rotational support of the galaxy at  $2.2h_R$ . In the following analysis, we define a galaxy to have a maximal disk if it has a baryonic mass (disk and bulge) contribution to the observed rotation curve of  $> 90\%$  at  $2.2h$ , or similarly, a dark matter contribution to the observed rotation curve of  $< 10\%$  at  $2.2h$ . We choose to adopt this definition of maximal disk over that of Sackett (1997) since we perform detailed bulge-disk decompositions, and are therefore able to model the combined bulge plus disk baryonic rotation curves. Furthermore, we use  $h$



measured at  $K$ , and when  $K$ -band imaging is unavailable, we use  $H$ . Since near-infrared bands trace most of the mass of the stellar populations, a near-infrared scale-length is more analogous to the stellar mass scale-length of a disk. Disk scale-lengths measured at  $K$  are typically  $\sim 1.2$  times shorter than those measured at  $B$  (de Jong 1996).

In Figure 3, there are 4 galaxies that have submaximal disks, even if the  $-0.1$  dex scatter in the color- $M/L$  relations is taken into account. Since the normalization of the color- $M/L$  relations is an upper limit, the number of galaxies in our sample that do not have maximal disks can in principle be much greater than 4. However, for those galaxies that we observe to have maximal disks, the overall shapes<sup>4</sup> of the inner parts of their observed rotation curves (within  $\sim R_{25}$ ) are generally matched by the shapes of their baryonic rotation curves. This is evidence that many of the disks have a significant baryonic component in their inner parts.

These 4 galaxies are NGC 3319<sup>5</sup>, NGC 3992, NGC 4062, and NGC 7606; they have baryonic mass contributions to their total masses at  $2.2h_{IR}$  of 22%, 50%, 57%, and 68%, respectively. In Figure 9 we plot for these 4 galaxies the baryonic rotation curves with and without uncertainties in distances and the color- $M/L$  relations taken into account; these baryonic rotation curves still under-predict the observed rotation curves for NGC 3319, NGC 3992, and NGC 4062. However, for

<sup>4</sup>This is distinguished from the “bumps and wiggles” of the observed rotation curves that are likely due to small-scale features such as bars and spiral arm perturbations (Palunas & Williams 2000; Kranz, Slyz, & Rix 2003; Slyz, Kranz, & Rix 2003).

<sup>5</sup>For NGC 3319, we do not take into account its innermost 2 observed rotation curve points since they are measured from H I and are likely affected by beam-smearing. Also, the distance measurement for NGC 3319 is from Cepheid variable stars and has an uncertainty of only  $\sim 10\%$ .

NGC 7606, the baryonic rotation curve that takes into account both these effects follows the observed rotation curve fairly well. For NGC 4062, its distance was calculated using a Virgocentric infall calculation and was found to be triple-valued (Paper I). We create baryonic rotation curves for NGC 4062 with the other 2 distance solutions (17.6 and 24.4 Mpc), both of which are greater than the one chosen in Paper I; they are plotted in Figure 9. These baryonic rotation curves have a strange behavior since they under-predict the observed rotation curve in the inner parts, but match it in the outer regions. This may be the effect of such factors as an underestimate of the stellar mass in the inner parts of the galaxy due to blue spiral arms in the  $B$ -band image (see image in Figure 1 of Paper I), a poor bulge/disk decomposition, and/or an underestimate of the uncertainties of the observed rotation curve. In summary, while NGC 4062 and NGC 7606 may not have submaximal disks, NGC 3319 and NGC 3992 likely do.

There are a few galaxies that have marginally submaximal disks. For these galaxies, the baryonic rotation curves for the  $+0.1$  dex scatter in the color- $M/L$  relations result in maximal disks. These galaxies are NGC 1241, NGC 2139, and NGC 2280, and they have baryonic mass contributions to their total rotational support at  $2.2h_{IR}$  of 75%, 73%, and 72%, respectively.

One striking example of a galaxy that is likely close to maximum disk is NGC 157. This galaxy has H $\alpha$  and H I rotation curves that have a sudden steep decline at  $\sim 8$ kpc ( $\sim 3h_K$ ) and flatten afterward, which results in a hump-like structure. While this peculiar behavior cannot be absolutely confirmed by Ryder et al. (1998), there are strong lines of evidence presented in their paper that point to this hump-like structure as physical. This same structure is also found in the baryonic

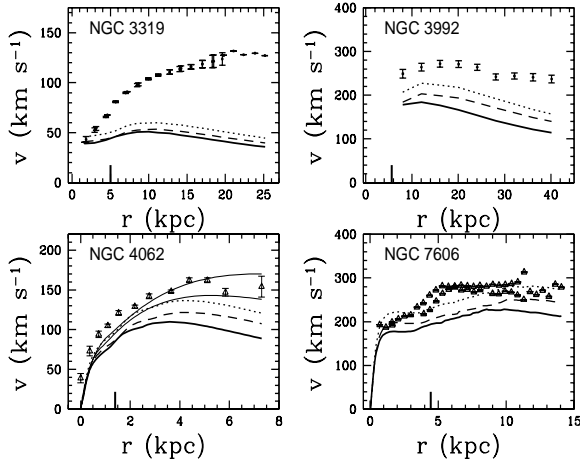


Fig. 9.— Same as Figure 8, but for galaxies where the baryons under-predict the observed rotation curves, and for the  $+0.1$  dex scatter in the color- $M/L$  relations and the  $+20\%$  distance uncertainty. For NGC 4062, baryonic rotation curves derived for 2 different distance determinations are plotted as thin solid lines.

rotation curve for NGC 157. Moreover, a dark matter halo in the shape of a NFW model is not consistent with this structure unless baryons make a significant contribution to the inner  $\sim 5$  scale-lengths of NGC 157. In summary, although a lower normalization of the IMF cannot be ruled out, it seems unlikely that at least NGC 157 is strongly submaximal.

## 6. Dark and Baryonic Matter Scaling Relations

In this section, we examine scaling relations for dark and baryonic matter. We use quantities from Tables 1 and 4 of Paper I, and derive others:  $V_{tot,max}$  the maximum observed rotation curve velocity,  $V_{b,max}$  the maximum baryonic rotation curve velocity,  $R(V_{b,max})$  the radius at which  $V = V_{b,max}$ , and  $M_b$  the baryonic mass. These quantities are listed in Table 2, and if they are derived from the baryonic

mass distributions, we also tabulate the differences in their values for renormalizations of the color- $M/L$  relations by  $\pm 0.1$  and  $-0.3$  dex. We choose to create the quantity  $V_{b,max}$  because it can be derived from imaging alone and obviates the need for much more expensive and time-consuming line width observations needed to obtain  $V_{tot,max}$ . For bright spirals,  $V_{b,max}$  should not differ from  $V_{tot,max}$  by very much, and due to the flat and usually noisier nature of the observed rotation curves, the measurement of  $V_{b,max}$  is more straightforward than that of  $V_{tot,max}$ . This quantity will be discussed further in §6.2.

We derive two quantities from the dark matter rotation curves calculated in §4.2:  $R_{10}$ , the radius where dark matter contributes 10% to the velocity of the observed rotation curve, and  $R_X$ , the radius where the dark matter contribution equals that of the baryons (the “cross-over radius”). The quantity  $R_{10}$  is similar to  $R_{IBD}$  of Salucci (2001) and  $R_t$  of Persic et al. (1996). The radius  $R_X$  is analogous to  $R_{2:1}$  of McGaugh & de Blok (1998). The radii  $R_{10}$  and  $R_X$  are listed in Table 2 along with the difference in values for renormalizations of the color- $M/L$  relations by  $\pm 0.1$  and  $-0.3$  dex. Note that for some galaxies we cannot measure  $R_{10}$  or  $R_X$ ; this is in general because their rotation curves do not extend far enough in radius.

### 6.1. Baryonic Scaling Relations

In Figure 10, basic physical parameters of galaxies are plotted versus  $M_b$ : total absolute  $B$  and  $K$ -band magnitudes, Hubble T-type,  $R_{25}$ , and  $B$  and  $K$ -band central surface brightnesses ( $\mu_{o,B}$ ,  $\mu_{o,K}$ ). They have the following correlation coefficients: 0.91 ( $B$ ), 1.00 ( $K$ ), 0.40 (Hubble T-type), 0.78 ( $R_{25}$ ), 0.29 ( $\mu_{o,B}$ ), and 0.58 ( $\mu_{o,K}$ ). Integrated magnitudes, sizes,  $\mu_{o,K}$ , and maximum rotation velocities correlate very well with  $M_b$ , such that galaxies with greater  $M_b$  are brighter, larger,

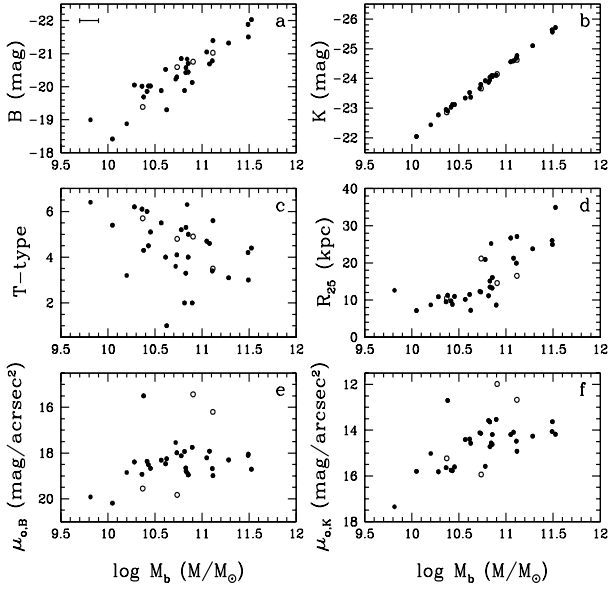


Fig. 10.— Basic physical parameters of galaxies versus baryonic mass. Open circles represent galaxies from the SDSS that have partial imaging. A typical error bar for  $M_b$  is plotted in panel a; error bars for the other quantities are the size of the data points at the resolution of the figure. To make the plot in panel c such that points do not overlap, we add fractions with values  $< 1$  to the integer Hubble T-types.

and have brighter  $\mu_{o,K}$ . Morphology and  $\mu_{o,B}$  also correlate with  $M_b$ , but to a lesser extent.

In Figure 11, relations are plotted for  $\log_{10}V_{b,max}$  and  $\log_{10}V_{tot,max}$ , which trace the baryonic and total mass components of the galactic potential, respectively. In Figure 11a, along the lines of Roberts & Haynes (1994), we plot  $\log_{10}V_{tot,max}$  versus  $\log_{10}L_B$  and find good agreement with their results. In Figure 11b, we plot  $\log_{10}V_{b,max}$  versus  $\log_{10}V_{tot,max}$ ; they are strongly correlated with a correlation coefficient of 0.82. These velocities should be equivalent for maximal disks, which many of the galaxies in our sam-

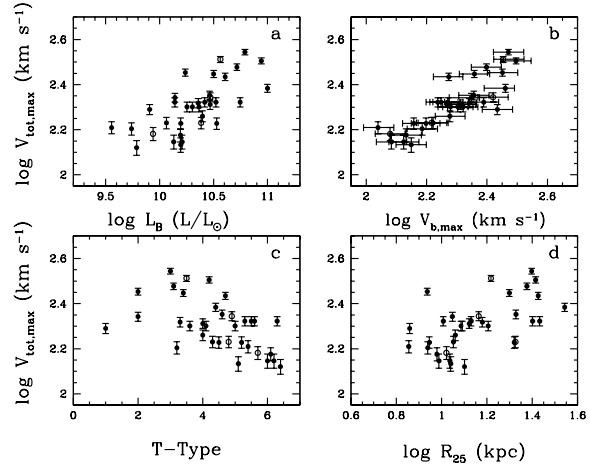


Fig. 11.— Relations for  $V_{tot,max}$  and  $V_{b,max}$ , which trace the total and baryonic mass component of the galactic potential, respectively. Open circles represent galaxies from the SDSS that have partial imaging. Error bars for T-type,  $L_B$ , and  $R_{25}$  are the size of the data points at the resolution of the figure.

ple have. In addition, a tight correlation indicates that there is not a wide spread in the degree of maximality. The quantity  $\log_{10}V_{tot,max}$  also correlates with Hubble T-type and  $R_{25}$  such that galaxies that rotate faster have earlier T-types and are larger. The quantity  $R(V_{b,max})$  correlates with  $\log_{10}M_b$  with a correlation coefficient of 0.66, but correlates relatively weakly with  $\log_{10}V_{b,max}$ ,  $\log_{10}V_{tot,max}$ , and  $\mu_{o,K}$  with correlation coefficients of 0.08, 0.35, and 0.16, respectively.

As discussed above, the maximum rotation speeds predicted from the baryon distributions are tightly correlated with the observed maximum rotation speeds. To examine this relation further, we plot the ratio of  $V_{b,max}$  to  $V_{tot,max}$  versus  $\mu_{o,K}$  in Figure 12, and find root mean square (rms) deviation from unity of only 0.18. Using this result, one can create a Tully-Fisher relation from two passband surface photometry and a redshift alone (e.g.,

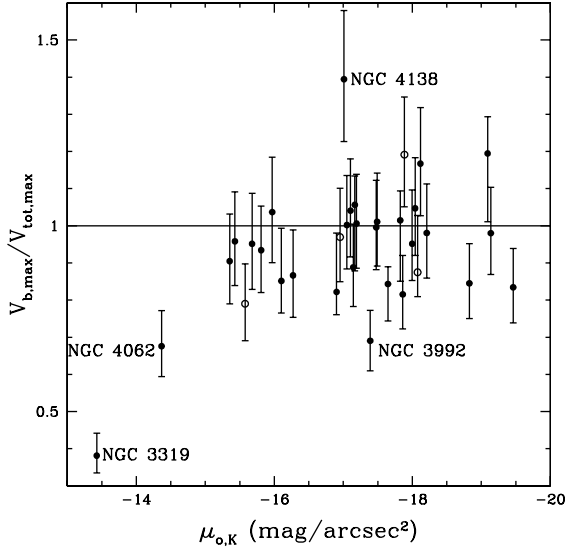


Fig. 12.— Ratio of maximum baryonic velocity to maximum observed velocity versus  $\mu_{o,K}$ . SDSS galaxies with partial imaging are plotted as open circles. Outliers are labeled: NGC 4062 and NGC 3992 have submaximal disks, NGC 4138 has evidence of kinematic disturbance, and NGC 3319 has both a submaximal disk and a kinematic disturbance.

by using the SDSS and the color- $M/L$  relations for  $g-r$  and  $(M/L_r)_*$ . The 4 outliers in Figure 12 are galaxies that have submaximal disks and/or are kinematically disturbed. The relation between  $V_{b,max}$  and  $V_{tot,max}$  is not expected to be as tight for less luminous spirals, but could possibly be calibrated for such a population.

In Figure 13a,b we plot the baryonic Tully-Fisher relations for  $V_{tot,max}$  and  $V_{b,max}$ . Weighted bisector fits are given in the form:  $M_b = M_{200}V^\alpha$  where  $M_{200}$  is the stellar mass in units of  $10^{10}M_\odot$  for a galaxy on the Tully-Fisher relation with  $V = 200 \text{ km s}^{-1}$ . They are:  $M_{200} = 5.40 \pm 0.03$  and  $\alpha = 3.4 \pm 0.3$  with a rms residual of 0.20 for  $V_{tot,max}$ , and  $M_{200} = 6.98 \pm 0.03$  and  $\alpha = 2.8 \pm 0.3$  with a rms residual of 0.22 for  $V_{b,max}$ . If we

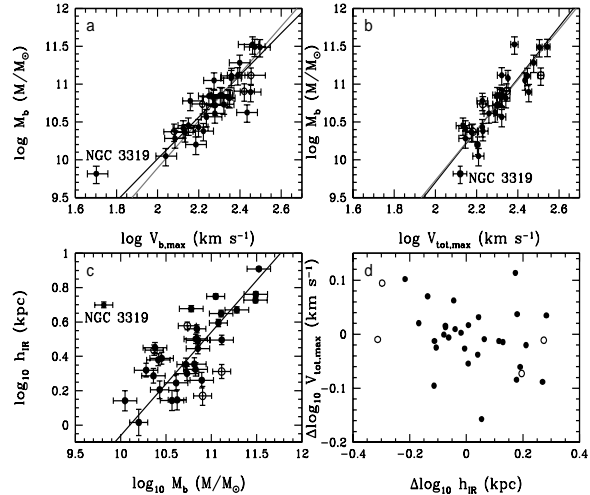


Fig. 13.— Baryonic Tully-Fisher relations for  $V_{tot,max}$  and  $V_{b,max}$ , and the size-baryonic mass relation are plotted in panels a-c. Weighted bisector fits with and without NGC 3319 are plotted as black and gray lines, respectively. In panel d, the  $V_{tot,max}$  residual of the Tully-Fisher relation is plotted versus the size residual from the size-baryonic mass relation. Galaxies from the SDSS that have partial imaging are plotted as open circles.

do not include the outlier in these two relations, NGC 3319, we obtain the following fits:  $M_{200} = 5.36 \pm 0.03$  and  $\alpha = 3.3 \pm 0.3$  with a rms residual of 0.19 for  $V_{tot,max}$ , and  $M_{200} = 6.75 \pm 0.03$  and  $\alpha = 3.1 \pm 0.3$  with a rms residual of 0.21 for  $V_{b,max}$ . The galaxy NGC 3319 is both kinematically disturbed on one side (Moore & Gottesman 1998), and has the smallest stellar mass in our sample. For most of the galaxies in our sample, we do not have H I or molecular hydrogen measurements. If gas masses were included, the Tully-Fisher slope of  $M_b$  on  $V_{tot,max}$  would flatten, as lower mass galaxies (e.g., NGC 3319) have a larger gas content than more massive galaxies (e.g., Verheijen 1997).

We refrain from comparing the slopes found here and in the literature (e.g., Bell & de Jong 2001; McGaugh 2005; Pizagno et al. 2005) for the following reasons. Such fits are sensitive, among other things, to the velocity measurements used (i.e.,  $V_{tot,max}$ ,  $V_{b,max}$ ,  $V_{flat}$ ,  $V_{2.2}$ ,  $W_{20}$ ), the range in stellar mass of the samples, and the galaxy samples used (range in Hubble type, field versus cluster environments). In particular, Gurovich et al. (2005) find a break in the stellar mass and baryonic Tully-Fisher relations for less massive galaxies ( $10^{7.6} \lesssim M_* \lesssim 10^{9.6} M_\odot$ ). This break is such that the Tully-Fisher relation for less massive galaxies is steeper than that for galaxies with stellar masses from  $\sim 10^{9.6}$ – $10^{11.2} M_\odot$ . Gurovich et al. (2005) find slopes for the lower and upper mass ranges of their  $H$ -band sample, using  $W_{20}$  as a velocity measurement, of  $4.4 \pm 0.3$  and  $3.3 \pm 0.3$ , respectively. This break/curvature makes a comparison between slopes of different samples risky at best, especially when different selection criteria are used. A 2D Kolmogorov-Smirnov test would be ideal, but beyond the scope of this work considering the modest stellar mass range of our sample.

The size-baryonic mass relation, where size is parameterized by  $h_{IR}$ , is plotted in Figure 13c. We perform a weighted bisector fit and find  $h_{IR} = 0.67 \pm 2.31 (M_b/10^{10} M_\odot)^{0.60 \pm 0.08}$  kpc with a rms of 0.16. We compare the  $V_{tot,max}$  residuals of the Tully-Fisher relation with the size residuals of the size-mass relation in Figure 13d, and find a scatter plot. If galaxy disks are maximal and the dark matter halos of galaxies of different surface brightness are identical, then it is predicted by McGaugh & de Blok (1998) and Courteau & Rix (1999) that there should be a correlation between these residuals. Courteau & Rix (1999) argue that the lack of residual correlation, essentially the surface brightness independence of the Tully-Fisher relation, implies that all

disks are submaximal. This argument, however, is not entirely straightforward, since in the Pizagno et al. (2005) model for disk collapse within a halo, variations in dark matter halo parameters can create enough scatter in the Tully-Fisher relation to hide the predicted correlation. Furthermore, McGaugh & de Blok (1998) and Sellwood (1999) argue that submaximal disks do not solve the problem, and one is left with a fine-tuning problem: either disk  $M/L$ s correlate with surface brightness, halo contributions vary, or Newtonian dynamics falters. Figure 12 illustrates this fine-tuning problem by showing that  $V_{b,max}/V_{tot,max}$  is independent of surface brightness, so that the total velocity “knows about” the baryonic contribution. Changing the normalization of the color- $M/L$  relations re-scales the y-axis of the plot, but the ratio remains independent of surface brightness.

## 6.2. Dark Matter Scaling Relations

In Figures 14a–d and 15, the baryon/dark matter equality radius in units of the disk scale length,  $R_X/h_{IR}$ , is plotted versus a number of galactic parameters:  $V_{tot,max}$ ,  $V_{b,max}$ , Hubble T-type,  $M_b$ ,  $B$ ,  $K$ ,  $\mu_{o,B}$ , and  $\mu_{o,K}$ . In Figure 14e, we plot  $R_X$  versus  $h_{IR}$ . There are fewer points in these figures than in previous ones since not all galaxies have a dark matter rotation curve that allows us to determine  $R_X$ . The correlation coefficients for these relations and for  $R(V_{b,max})$  with  $R_X$  are listed in Table 4. The radius  $R_X$  is found to correlate most strongly with  $V_{b,max}$  and very strongly with  $M_b$ , Hubble T-type, and  $V_{tot,max}$ . There are no changes in the relative strengths of the relations if the color- $M/L$  relations are renormalized by  $\pm 0.1$  or  $-0.3$  dex.

The trends with  $R_X$  that we find are qualitatively in agreement with those in the literature (e.g., de Blok & McGaugh 1997; McGaugh & de Blok 1998; Pizagno et al. 2005), with some exceptions that are discussed here.

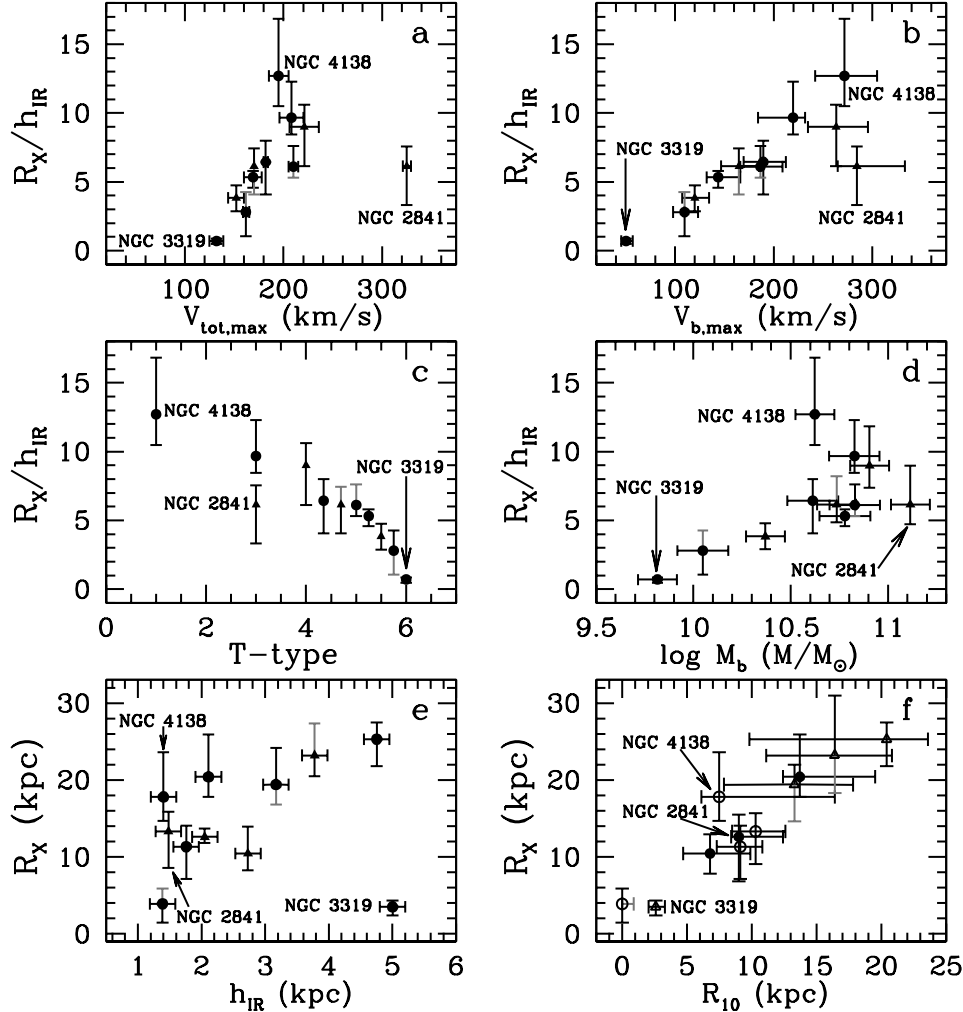


Fig. 14.— Relations for  $R_X/h_{IR}$  and  $R_X$ . In panels a–e, triangles represent galaxies from SDSS that only have partial imaging. Error bars represent the values of the quantities derived by renormalizing the color- $M/L$  relations by  $\pm 0.1$  dex; upper and lower limits to these values are plotted in gray. To make the points in panel c such that they do not overlap, we add fractions with values  $< 1$  to the integer Hubble types. In panel f, galaxies are plotted with different symbols according to their  $h_{IR}$ : those with  $h_{IR} < 1$  kpc as open circles, those with  $1 \text{ kpc} \leq h_{IR} < 3$  kpc as filled circles, and those with  $3 \text{ kpc} \leq h_{IR}$  as open triangles. The galaxies NGC 2841, NGC 3319, and NGC 4138 are labeled in all panels; they have evidence of kinematical disturbances despite their normal appearances. The three outliers in Figures 14 and 15 are NGC 2841, NGC 3319, and NGC 4138. Despite their normal optical morphologies, these galaxies have signatures of kinematic disturbances. The galaxy NGC 2841 has a warp in its outer H I disk (Bosma 1981) and an indication of a counter-rotating stellar component for  $5'' \leq r \leq 12''$  (Silchenko, Vlasyuk, & Burenkov 1997). Similarly, NGC 4138 has both a counter-rotating disk and a significant warp in its outer H I disk (Jore, Broeils, & Haynes 1996). This warp may be the cause of the decline of its H I rotation curve, and hence what makes this galaxy an outlier. The third outlier, NGC 3319, is discussed in §6.1.

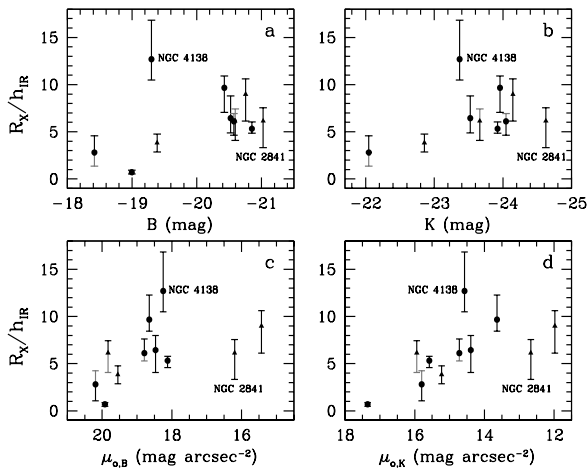


Fig. 15.— Relations for  $R_X/h_{IR}$  and integrated magnitudes and central surface brightnesses. Symbols and error bars are the same as in Figure 14. The galaxy NGC 3319 has a  $\mu_{o,K}$  measurement, but not a  $K$  measurement. Error bars along the x-axis are approximately the point size at the resolution of the plot.

McGaugh & de Blok (1998) and de Blok & McGaugh (1997) find that  $\mu_{o,B}$  plays a major role in relations with galaxy properties, including with  $R_{2:1}$ , which is analogous to our  $R_X$  parameter. We find that  $R_X/h_{IR}$  is correlated with  $\mu_{o,B}$ , but that it is even more correlated with  $\mu_{o,K}$ . We do not find a correlation between the mass discrepancy and  $\mu_{o,K}$  (in Figure 12 we plot the inverse mass discrepancy), but McGaugh & de Blok (1998) do find a relation between total  $M/L_B$  at  $4h$  and  $\mu_{o,B}$ . Also, we find that  $h_{IR}$  correlates strongly with  $R_X$ , once outliers are removed, which is not in qualitative agreement with other studies: McGaugh & de Blok (1998) and Zavala et al. (2003) find that  $h$  does not correlate with total  $M/L_B$  evaluated at  $4h$  or the mass discrepancy evaluated at maximum rotation velocity, respectively. However, the results of Pizagno et al. (2005) for relations with  $h$  are consistent

with ours; they find that more compact galaxies have a larger mass discrepancy (measured at  $2.2h_i$ ) than larger galaxies. Zavala et al. (2003) find a number of relations involving a quantity similar to the mass discrepancy that are in contradiction to those presented in this paper and in the literature.

Here we discuss possible causes of these discrepancies. Our differences with McGaugh & de Blok (1998) may be traced to the quantities used in the analyses: they use  $M/L_B$  and  $h_B$ , while we use  $R_X$  and  $h_{IR}$ . Luminosity in the  $B$ -band should have more scatter in relations with galaxy properties than baryonic mass derived from a combination of optical and near-infrared data. This is because the  $B$ -band is more affected by star formation and extinction, while the  $K$ -band is a better tracer of stellar mass. In addition, a near-infrared scale-length is more analogous to the baryonic mass scale-length of a disk, and hence should have less scatter in its relations with galaxy properties than an optical scale-length. Adding some credence to the hypothesis that different quantities are the root of the discrepancy, McGaugh & de Blok (1998) find that relations between  $R_{2:1}$  and both  $\mu_{o,B}$  and  $M_B$  are such that brighter galaxies have larger values of  $R_{2:1}$ , consistent with our results. That McGaugh & de Blok (1998) find a correlation between  $M/L_B$  evaluated at  $4h$  and  $\mu_{o,B}$  is likely also due to the larger range in surface brightness in their sample.

In Figure 14f,  $R_{10}$  is plotted versus  $R_X$ , and galaxies are plotted as different symbols according to their value of  $h_{IR}$ . Although there is some scatter, as  $h_{IR}$  increases, these two radii move further out in the disks in tandem. That there is such a tight relation between  $R_{10}$  and  $R_X$  tells us that dark matter contributions to the observed rotation curves must increase in a characteristic way between these two radii for all galaxies. This is likely due to the combined effects of quasi-exponential

disks and observed rotation curves that are nearly flat. If this is correct, then  $R_{10}$  should have more scatter in its relations with galaxy properties than  $R_X$  because the observed rotation curves should not yet be flat in the region where  $R_{10}$  is measured, which is found to be the case.

## 7. Radial Behavior of Dark Matter

In Figure 16, the dimensionless parameter  $\beta(r) \equiv M_b(r)/M_{tot}(r)$ , where  $M_b$  is the baryonic mass, and its inverse are plotted for galaxies with an appreciable dark matter contribution. It measures the fractional contribution of baryons to the gravitational potential as a function of radius in a galaxy, and is akin to the  $\beta$  parameter defined by Salucci (2001) and similar parameters used in many other papers, except here it is evaluated at all radii. Where  $\beta(r) = 1$ , the baryonic mass of a galaxy accounts for its observed rotation curve,  $\beta(r) = 0.5$  at  $r = R_X$ , and  $\beta(r) = 0$  where the dark matter accounts for its observed rotation curve. If the baryonic model over-predicts the observed rotation curve, then  $\beta(r) > 1$ . In Figure 16a,  $\beta(r)$  is plotted versus radius in terms of  $h_{IR}$ . For many galaxies, the observed rotation curves are entirely accounted for by baryons in the inner parts. Beyond this region, baryonic mass falls off as dark matter begins to dominate. Other galaxies are dark matter dominated throughout. Curves in Figure 16a have different line types that correspond to ranges of  $V_{b,max}$ . For most of the galaxies, as  $V_{b,max}$  increases, so does the proportion of baryonic to dark matter at all radii such that the fastest rotators are observed to be dominated by baryons until quite far out into their disks. However, there is clearly much scatter about this trend; this conclusion can also be inferred from Figure 14f.

In Figure 16b,  $\beta(r)$  is plotted versus radius in units of  $R_X$ . This choice of radial coordi-

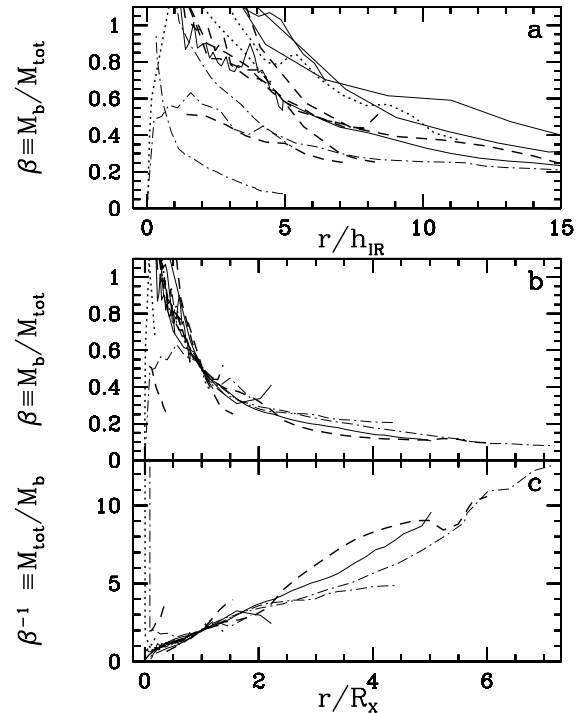


Fig. 16.—  $\beta(r) \equiv M_b(r)/M_{tot}(r)$  and its inverse for galaxies with an appreciable dark matter contribution.  $\beta(r)$  is plotted versus  $r/h_{IR}$  and  $r/R_X$  in parts a and b, respectively; its inverse is plotted versus  $r/R_X$  in panel c. Different line types correspond to the  $V_{b,max}$  of the galaxies:  $V_{b,max} > 250$  km s $^{-1}$  (solid line),  $201 < V_{b,max} \leq 250$  (dotted line),  $120 < V_{b,max} \leq 201$  (dashed line), and  $V_{b,max} \leq 120$  (dot-dash line line).

nate causes the curves to overlap at  $r = R_X$  (where  $\beta(r) = 0.5$ ), and thus allows for a better comparison of their radial behavior. In Figure 16c, we plot the somewhat less intuitive function  $\beta^{-1}(r)$  since it increases linearly with  $r/R_X$ . There is little variation in the behavior of the curves in Figures 16b,c. Such regularity can be explained in terms of quasi-exponential disks and flat rotation curves as follows: The rotation curve of a galaxy is nearly flat beyond  $r \sim 2h_{IR}$ , or it is at least a slow function of  $r$  and varies less than  $V_b(r)$  in this region. In addition, much of the bary-



onic mass of a galaxy is enclosed at  $r \sim 2h_{IR}$ , which causes the baryonic rotation curves to be roughly Keplerian ( $V_b(r) \propto 1/r$ ) beyond this radius. Therefore, for all galaxies, beyond  $\sim 2h_{IR}$ , it should be the case that  $\beta(r) \equiv V_b^2/V_{tot}^2 \propto 1/r$ , which is what we observe. All the  $\beta(r)$  curves overlap nicely when plotted versus radius normalized to  $R_X$  since this radius is located beyond  $2h_{IR}$ , and is generally in the falling part of the baryonic rotation curves. We parametrize the trend of  $\beta^{-1}$  with  $r/R_X$  in a simple universal manner that holds for all galaxies:  $\beta^{-1} = 1.71(r/R_X) + 0.021$ .

This relation is consistent with the prediction of Palunas & Williams (2000) that either the contribution of dark matter within the optical radius of galaxies is small or that the distribution of dark matter is coupled to that of the luminous matter. This relation is also similar in spirit to the parameterization of the mass discrepancy-acceleration relation of McGaugh (2004). Since  $\beta^{-1}$  is the mass discrepancy, and  $a = V^2/r \propto 1/r$  for flat rotation curves, a natural mass discrepancy-acceleration relation arises.

## 8. Comparison With Theories of Halo Density Distributions

We compare the derived dark matter profiles with an analytical function designed to parametrize the density profile of dark matter halos in N-body simulations. In particular, we compare our data to the NFW formulation for dark matter halo density profiles (Navarro, Frenk, & White 1996) with and without taking into account adiabatic contraction of the halos. To do this, for each galaxy, we fit its observed rotation curve with a total mass rotation curve created from the addition of its baryonic rotation curve to a grid of halo models, with a reduced  $\chi^2$  statistic. Uncertainties in the observed rotation curves are taken to be  $10 \text{ km s}^{-1}$ ; results do not differ significantly if the error bars plotted in Figure 3 are

used. To test the most common implementation of dark matter contraction (Blumenthal et al. 1986), we adiabatically contract the grid of halo models according to the radial density distribution of baryons in the galaxies following the formalism of Dutton et al. (2005), and perform the fits again. The NFW fitting formula has 2 free parameters that we fit for using a grid covering:  $0.5 \leq c_{200} \leq 20$  and  $0.5 V_{tot,max} \leq V_{200} \leq 2.5 V_{tot,max}$ .

In Figure 17, we plot the best-fit halo models for 8 example galaxies, and in Table 3 we list the best-fit parameters along with the reduced  $\chi^2$  of all the fits. Most of the fits are very poor; the average reduced  $\chi^2$  values with and without adiabatic contraction are: 7.1 and 4.2 for the original color- $M/L$  relations, 14.0 and 7.3 for the +0.1 dex renormalization of the color- $M/L$  relations, 4.8 and 3.4 for -0.1 dex, and 3.9 and 4.3 for -0.3 dex. We do not perform fits for galaxies when most of the observed rotation curve is accounted for by the baryonic rotation curve.

For baryonic rotation curves derived from the original color- $M/L$  relations, nearly all fits to the NFW models without contraction have a smaller reduced  $\chi^2$  than those where contraction was performed. The exceptions are NGC 4062 and NGC 3992, which likely have submaximal disks. For galaxies that have a large baryonic contribution to the inner parts of their rotation curves, adiabatic contraction over-contracts the inner parts of their dark matter halos such that the resulting total mass rotation curves over-predict the measured rotation curves, as in Weiner, Sellwood, & Williams (2001), for example. For fits to the NFW models where the baryonic rotation curves were derived from color- $M/L$  relations that were renormalized by +0.1 dex, the situation is exactly the same. For -0.1 dex, 7 galaxies have better fits when contraction is taken into account, and for -0.3 dex, 15 galaxies have a better fit. This implementation of dark mat-

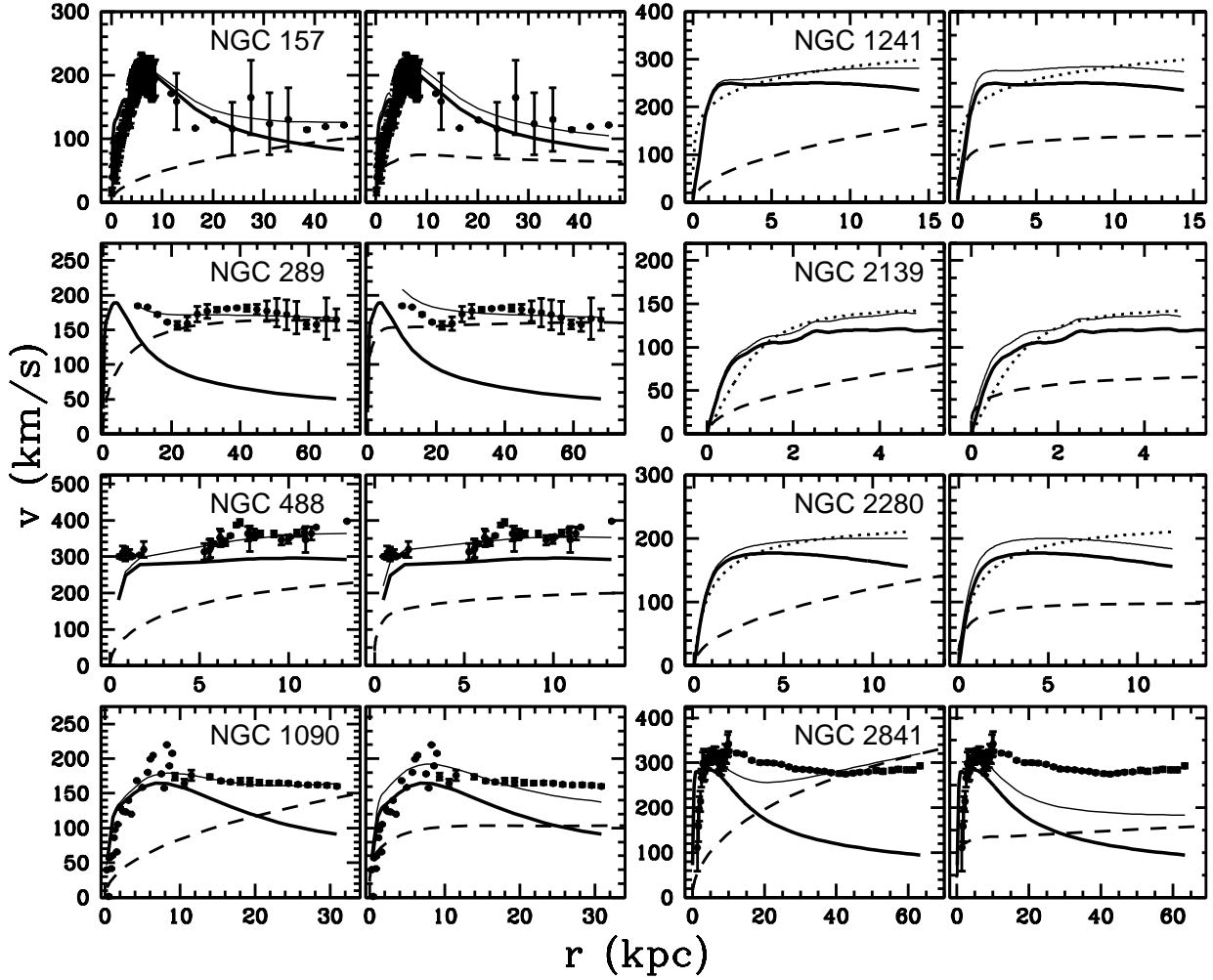


Fig. 17.— NFW halo fits for 8 example galaxies without (left) and with (right) adiabatic contraction. Best-fit NFW models are plotted as dashed lines, baryonic rotation curves as thick solid lines, total rotation curves (sums of the best-fit NFW models and the baryonic rotation curves) as thin solid lines, and observed rotation curves as points. For those galaxies with a rotation curve from Mathewson et al. 1992 that is modeled by Courteau 1997, we only plot the model as a dotted line for clarity.

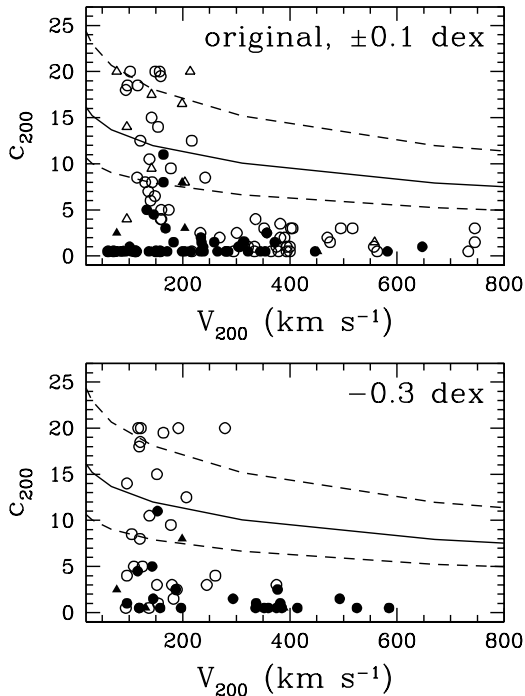


Fig. 18.— Best-fit parameters for NFW fits with and without adiabatic contraction (filled and open symbols, respectively). The median and the 68 per cent of the  $c_{200}$  values measured in numerical N-body simulations of dark matter halos are plotted as solid and dashed lines, respectively. When the best-fit halo is at the edge of the parameter space searched, it is plotted as a triangle, otherwise it is plotted as a circle. In part a, best-fit parameters for the original and  $\pm 0.1$  dex renormalizations of the color- $M/L$  relations are plotted; in part b, best-fit parameters for the  $-0.3$  dex renormalization are plotted.

ter contraction works best when baryons do not account for all of the inner parts of the observed rotation curve.

In Figure 18, we plot the best-fit values of  $V_{200}$  and  $c_{200}$  and the range of these parameters found in N-body simulations (Bullock et al. 2001; Eke, Navarro, & Steinmetz 2001). Even under the assumption of no adia-

batic contraction, the derived concentrations for these halos are low compared to those measured from simulations. The concentrations for  $-0.3$  dex are in slightly better agreement with simulations, but are still quite low. In concert with this, McGaugh, Barker, & de Blok (2003) and McGaugh (2004) found concentrations for NFW halos that are too low for a standard  $\Lambda$ CDM universe. In addition, Alam, Bullock, & Weinberg (2002) examined low surface brightness galaxies and found their dark matter halos to be under-concentrated compared to what is expected from a standard  $\Lambda$ CDM universe, even if they assumed the galaxies to be dark matter-dominated.

## 9. Summary

We have decomposed the rotation curves of 34 nearby bright spiral galaxies into baryonic and dark matter components by applying color- $M/L$  relations to near-infrared and optical photometry, and find the following:

- The dark-to-luminous matter distributions are self-similar once scaled by  $R_X$ , the radius where the baryonic and dark matter contributions to the rotation curve are equivalent. This behavior is parameterized by a simple function whose form is due to the quasi-exponential nature of galaxy disks and rotation curves that are nearly flat after an initial rise. This result is independent of the normalization of the color- $M/L$  relations.
- The radii  $R_{10}$  and  $R_X$ , where dark matter contributes 10% and 50% to the rotation of galaxies, respectively, correlate with galaxy properties. The strongest correlation with  $R_X$  is with the maximum baryonic rotation speed such that galaxies with  $R_X$  measurements that lie further out in their disks

rotate faster. The next strongest correlations are equivalently baryonic mass, observed rotation speed, and Hubble T-type. Contrary to what is expected from previous studies (de Block & McGaugh 1998; Zavala et al. 2003), *B*-band central surface brightness is not found to be the main driving force in relations with  $R_X$  for this sample of bright galaxies. The radii  $R_X$  and  $R_{10}$  move out in galaxy disks in tandem, consistent with a self-similar dark-to-luminous matter distribution among galaxies.

- We confirm the normalization of the color- $M/L$  relations given in Bell et al. (2003), which is analogous to an upper limit on the IMF based on the dynamics of disk galaxies. A more careful analysis of the data used in both Bell & de Jong (2001) and Bell et al. (2003) is performed, and data from this paper are included in the sample.
- All but 4 of the 34 galaxies in our sample are close to maximal disk. Two of these 4 galaxies have maximal disks within uncertainties. A prime example of a galaxy that cannot have a submaximal disk given the current formulations of dark matter halos is NGC 157 which has a pronounced hump-like structure in its observed and baryonic rotation curves.
- Maximum rotation velocities predicted from the baryon distributions of galaxies ( $V_{b,max}$ ) are tightly correlated with the observed maximum rotation speeds ( $V_{tot,max}$ ). Using this, a baryonic Tully-Fisher relation can be created based on two-passband surface photometry and a redshift alone (e.g., with the SDSS and color- $M/L$  relations for  $g-r$  and  $(M/L_r)_*$ , or for more distant redshift surveys with Hubble Space Telescope imaging). Such a relation could possibly

be calibrated for lower luminosity galaxies.

- We find generally poor fits for the NFW parameterization for dark matter halos due to the significant baryonic contributions found in the inner parts of most galaxies. The concentrations of the best-fit NFW halos are therefore much lower than what is expected for galaxies in a standard  $\Lambda$ CDM universe. This is even the case when the color- $M/L$  relations are renormalized by -0.3 dex. In order to have better fits, a normalization even lower than -0.3 dex, where baryons contribute very little to the total mass in the inner parts of rotation curves, would have to be implemented. Adiabatic contraction, as it is normally implemented, makes these fits worse by adding more dark matter to the inner parts of galaxies.

We would like to thank Richard Pogge, James Pizagno, James Bullock, Jay Frogel, Chris Kochanek, and David Weinberg for valuable discussions. The referee, Stacy McGaugh, is thanked for constructive comments that greatly improved the quality of this paper. We are grateful to the following authors who provided rotation curves in tabular form via email: Kor Begeman, Gianfranco Gentile, Thilo Kranz, Povilas Palunas, Stuart Ryder, Michele Thornley, and Wilfred Walsh. We are grateful to Marc Verheijen who made available his high-quality imaging and rotation curves of galaxies in the Ursa Major cluster. SAK would like to acknowledge financial support from The Space Telescope Science Institute Director's Discretionary Research Fund (DDRF). We thank the CTIO TAC for generous allocation of time for The Ohio State University Galaxy Survey and the many people over the years who helped collect these

observations. Funding for The Ohio State University Bright Spiral Galaxy Survey was provided by grants from The National Science Foundation (grants AST-9217716 and AST-9617006), with additional funding by The Ohio State University.

This paper makes use of data from both the Sloan Digital Sky Survey and the Two Micron All Sky Survey. The Two Micron All Sky Survey is a joint project of the University of Massachusetts and the Infrared Processing and Analysis Center/California Institute of Technology, funded by the National Aeronautics and Space Administration and the National Science Foundation. Funding for the creation and distribution of the SDSS Archive has been provided by the Alfred P. Sloan Foundation, the Participating Institutions, the National Aeronautics and Space Administration, the National Science Foundation, the U.S. Department of Energy, the Japanese Monbukagakusho, and the Max Planck Society. The SDSS Web site is <http://www.sdss.org/>. The SDSS is managed by the Astrophysical Research Consortium (ARC) for the Participating Institutions. The Participating Institutions are The University of Chicago, Fermilab, the Institute for Advanced Study, the Japan Participation Group, The Johns Hopkins University, Los Alamos National Laboratory, the Max-Planck-Institute for Astronomy (MPIA), the Max-Planck-Institute for Astrophysics (MPA), New Mexico State University, University of Pittsburgh, Princeton University, the United States Naval Observatory, and the University of Washington.

This research has made use of NASA's Astrophysics Data System, the NASA/IPAC Extragalactic Database (NED), and the HyperLeda database and the VizieR catalog access tool. NED that is operated by the Jet Propulsion Laboratory, California Institute of Technology, under contract with the National Aeronautics and Space Administration.

This research also made use of the HyperLeda database and the VizieR catalog access tool, CDS, Strasbourg, France.

## REFERENCES

- Abadi, M. G., Navarro, J. F., Steinmetz, M., & Eke, V. R. 2003, *ApJ*, 591, 499
- Abazajian, K. et al. 2004, *AJ*, 128, 502
- Alam, S. M. K., Bullock, J. S. & Weinberg, D. H. 2002, *ApJ*, 572, 34
- Begeman, K. G. 1987, Ph.D. thesis, Univ. Groningen
- Bell, E. F., McIntosh, D. H., Katz, N., & Weinberg, M. D. 2003, *ApJS*, 149, 289
- Bell, E. F. & de Jong, R. S. 2001, *ApJ*, 550, 212
- Binney, J., & Tremaine, S. 1987, *Galactic Dynamics* (Princeton : Princeton Univ. Press)
- Bizyaev, D. & Mitronova, S. 2002, *A&A*, 389,795
- Blais-Ouellette, S., Amram, P., Carignan, C., & Swaters, R. 2004, *A&A*, 420, 147
- Blumenthal, G. R., Faber, S. M., Flores, R., & Primack, J. R. 1986, *ApJ*, 301, 27
- Bosma, A. 1981, *AJ*, 86, 1791
- Broeils, A. H. 1992, Ph.D. thesis, Rijksuniversiteit Groningen
- Bullock, J. S. et al. 2001, *MNRAS*, 321, 559
- Buta, R. et al. 2001, *AJ*, 121, 225
- Cardelli, J. A., Clayton, G. C., & Mathis, J. S. 1989, *ApJ*, 345, 245
- Casertano, S. 1983, *MNRAS*, 203, 735
- Corradi, R. L. M., Boulesteix, J., Bosma, A., Amram, P., & Capaccioli, M. 1991, *A&A*, 244, 27

- Courteau, S. 1997, *AJ*, 114, 2402
- Courteau, S. & Rix, H.-W. 1999, *ApJ*, 513, 561
- Cutri, R. M., et al. 2000, Explanatory Supplement to the 2MASS Second Incremental Data Release (Pasadena: Caltech)
- McGaugh, S. S., & de Blok, W. J. G. 1997, *MNRAS*, 290, 533
- McGaugh, S. S., & de Blok, W. J. G. 1998, *ApJ*, 508, 132
- de Jong, R. S. 1996, *A&AS*, 118, 557
- Disney, M., Davies, J., & Phillipps, S. 1989, *MNRAS*, 239, 939
- Dutton, A. A., Courteau, S., de Jong, R., & Carignan, C. 2005, *ApJ*, 619, 218
- Eke, V., R., Navarro, J. F., & Steinmetz, M. 2001, *ApJ*, 554, 114
- Freeman, K. C. 1970, *ApJ*, 160, 811
- Fridman, A. M. et al. 2001, *A&A*, 371, 538
- Gentile, G., Salucci, P., Klein, U., Vergani, D., & Kalberla, P. 2004, *MNRAS*, 351, 903
- Giraud, E. 1998, *AJ*, 116, 1125
- Gordon, K. D., Misselt, K. A., Witt, A. N., & Clayton, G. C. 2001, *ApJ*, 551, 269
- Gurovich, S. et al. 2005, *Publications of the Astronomical Society of Australia*, 21, 412
- Holwerda, B. W., Gonzalez, R. A., Allen, R. J., & van der Kruit P. C. 2005, *AJ*, 129, 1396
- Ibata, R. et al. 2005, *ApJ*, submitted, astro-ph 0504164
- Jarrett, T. H., Chester, T., Cutri, R., Schneider, S. E., Huchra, J. P. 2003, *AJ*, 125, 525
- Jarrett, T. H., Chester, T., Cutri, R., Schneider, S., Skrutskie, M., & Huchra, J. P. 2000, *AJ*, 119, 2498
- Jore, K. P., Broeils, A. H., & Haynes, M. P. 1996, *AJ*, 112, 438
- Kassin, S. A., de Jong, R. S., & Pogge, R. W. 2005, *ApJS*, accepted (Paper I)
- Kranz, T. 2002, Ph.D. thesis, Universität Heidelberg
- Kranz, T., Slyz, A., & Rix, H.-W. 2003, *ApJ*, 586, 143
- Martin, P. G. & Whittet, D. C. B. 1990, *ApJ*, 357, 113
- Mathewson, D. S., Ford, V. L., & Buchhorn, M. 1992, *ApJS*, 81, 413
- McGaugh, S. S. & de Blok, W. J. G. 1998, *ApJ*, 499, 41
- McGaugh, S. S., Barker, M. K., & de Blok, W. J. G. 2003, *ApJ*, 584, 566
- McGaugh, S. S. 2004, *ApJ*, 609, 652
- McGaugh, S. S. 2005, *ApJ*, 632, 859
- Moore, E. M. & Gottesman, S. T. 1998, *MNRAS*, 294, 353
- Navarro, J. F., Frenk, C. S., & White, S. D. M. 1996, *ApJ*, 462, 563 (NFW)
- Palunas, P. & Williams, T. B. 2000, *AJ*, 120, 2884
- Persic, M. & Salucci, P. 1988, *MNRAS*, 234, 131
- Persic, M. & Salucci, P. 1990, *MNRAS*, 245, 577
- Persic, M., Salucci, P., & Stel, F. 1996, *MNRAS*, 281, 27
- Peterson, C. J. 1980, *AJ*, 85, 226

- Pizagno, J. 2005, *ApJ*, 633, 844
- Roberts, M. S. & Haynes, M. P. 1994, *ARA&A*, 32, 115
- Rubin, V. C., Burstein, D., Ford, W. K., Jr., & Thonnard, N. 1985, *ApJ*, 289, 81
- Rubin, V. C., Waterman, A. H., & Kenney, J. D. P. 1999, *AJ*, 118, 236
- Ryder, S. D. et al. 1996, *ApJ*, 460, 665
- Ryder, S. D., Zasov, A. V., Sil'chenko, O. K., McIntyre, V. J., & Walsh, W. 1998, *MNRAS*, 293, 411
- Sackett, P. D. 1997, *ApJ*, 483, 103
- Salucci, P. 2001, *MNRAS*, 320, L1
- Sanders, R. H. 1996, *ApJ*, 473, 117
- Sellwood, J. A. 1999, in *ASP Conf. Ser.* 182, *Galaxy Dynamics*, ed. D. Merritt, J. A. Sellwood, & M. Valluri (San Francisco: ASP), 351
- Sil'chenko, O. K., Vlasyuk, V. V., & Burenkov, A. N. 1997, *A&A*, 326, 941
- Slyz, A. D., Kranz, T., & Rix, H.-W. 2003, *MNRAS*, 346, 1162
- Sofue, Y. & Rubin, V. 2001, *ARA&A*, 39, 137
- Sparke, L. S. & Gallagher, J. S. 2000, *Galaxies In the Universe : An Introduction* (Cambridge, U.K.: Cambridge Univ. Press)
- Tully, R. B., Pierce, M. J., Huang, J.-S., Saunders, W., Verheijen, M. A. W. & Witchalls, P. L. 1998, *AJ*, 115, 2264
- Tummers, B. 2003, <http://www.nikhef.nl/~keeshu/datathief/>
- van Albada, T. S., Bahcall, J. N., Begeman, K. & Sancisi, R. 1985, *ApJ*, 295, 305
- van Albada, T. S. & Sancisi, R. 1986, *Philos. Trans. R. Soc. London*, 320, 447
- van der Hulst, J., Terlouw, J., Begeman, K., Zwitzer, W., & Roelfsema, P. 1992, in *ASP Conf. Ser.* 25, *Astronomical Data Analysis Software and Systems I*, ed. D. Worall, C. Biemesderfer, & J. Barnes (San Francisco: ASP), 131
- Verheijen, M. A. W. 1997, Ph.D. thesis, Rijksuniversiteit Groningen
- Walsh, W., Staveley-Smith, L., & Oosterloo, T. 1997, *AJ*, 113, 1591 & Firmani, C. 2003, *A&A*, 412, 633
- Weiner, B. J., Sellwood, J. A., & Williams, T. B. 2001, *ApJ*, 546, 931
- Zavala, J., Avila-Reese, V., Hernández-Toledo, H., & Firmani, C. 2003, *A&A*, 412, 633

TABLE 1

Galaxy	Tracer <sup>a</sup>	Reference(s)
NGC 157	FP H $\alpha$ , H I	Fridman et al. 2001, Ryder et al. 1998 <sup>b</sup>
NGC 289	H I	Walsh, Staveley-Smith, & Oosterloo 1997 <sup>b</sup>
NGC 488	H $\alpha$	Peterson 1980 <sup>b,c</sup>
NGC 908	H $\alpha$	Mathewson, Ford, & Buchhorn 1992
NGC 1087	H $\alpha$	Rubin et al. 1985
NGC 1090	H $\alpha$ , H I	Courteau 1997, Gentile et al. 2004
NGC 1241	H $\alpha$	Mathewson, Ford, & Buchhorn 1992
NGC 1385	H $\alpha$	Mathewson, Ford, & Buchhorn 1992
NGC 1559	H $\alpha$	Mathewson, Ford, & Buchhorn 1992
NGC 1832	H $\alpha$	Mathewson, Ford, & Buchhorn 1992
NGC 2090	H $\alpha$	Mathewson, Ford, & Buchhorn 1992
NGC 2139	H $\alpha$	Mathewson, Ford, & Buchhorn 1992
NGC 2280	H $\alpha$	Mathewson, Ford, & Buchhorn 1992
NGC 2841	FP H $\alpha$ , H I	Blais-Ouellette et al. 2004, Giraud 1998 <sup>c</sup>
NGC 3198	FP H $\alpha$ , H I	Corradi et al. 1991 <sup>b</sup> , van Albada et al. 1985
NGC 3223	H $\alpha$	Mathewson, Ford, & Buchhorn 1992
NGC 3319	H I	Moore & Gottesman 1998 <sup>b,c</sup>
NGC 3521	H I	Sanders 1996 <sup>c</sup>
NGC 3726	H I	Verheijen 1997 <sup>b</sup>
NGC 3893	H $\alpha$ , H I	Kranz 2002, Verheijen 1997 <sup>b</sup>
NGC 3949	H I	Verheijen 1997 <sup>b</sup>
NGC 3953	H I	Verheijen 1997 <sup>b</sup>
NGC 3992	H I	Verheijen 1997 <sup>b</sup>
NGC 4051	H I	Verheijen 1997 <sup>b</sup>
NGC 4062	H $\alpha$	Rubin et al. 1985
NGC 4138	N II, H I	Jore, Broeils, & Haynes 1996 <sup>c</sup> , Verheijen 1997 <sup>b</sup>
NGC 4651	H $\alpha$	Rubin, Waterman, & Kenney 1999
NGC 4698	H $\alpha$	Rubin, Waterman, & Kenney 1999
NGC 5371	H I	Begeman 1987
NGC 5806	H $\alpha$	Courteau 1997
NGC 6300	FP H $\alpha$ , H I	Buta et al. 2001, Ryder et al. 1996
NGC 7083	H $\alpha$	Mathewson, Ford, & Buchhorn 1992
NGC 7217	H $\alpha$	Rubin et al. 1985
NGC 7606	H $\alpha$	Mathewson, Ford, & Buchhorn 1992

<sup>a</sup>The notation “FP H $\alpha$ ” is used for rotation curves derived from Fabry-Perot measurements of H $\alpha$ .

<sup>b</sup>Errors are taken as the difference in velocity between the approaching and receding sides.

<sup>c</sup>The rotation curve has been extracted electronically from a plot in the referenced paper.



TABLE 2

Galaxy	Observed	Baryonic Matter			Dark Matter	
	$V_{tot,max}$ (km/s)	$V_{b,max}$ (km/s)	$R(V_{b,max})$ (kpc)	$M_b$ ( $10^{10} M_\odot$ )	$R_{10}$ (kpc)	$R_X$ (kpc)
		$\Delta_{+0.1dex}$		$\Delta_{+0.1dex}$	$\Delta_{+0.1dex}$	$\Delta_{+0.1dex}$
		$\Delta_{-0.1dex}$		$\Delta_{-0.1dex}$	$\Delta_{-0.1dex}$	$\Delta_{-0.1dex}$
		$\Delta_{-0.3dex}$		$\Delta_{-0.3dex}$	$\Delta_{-0.3dex}$	$\Delta_{-0.3dex}$
NGC 157	205	205	6.2	7.1	...	...
		+25		+1.8	...	...
		-22		-1.4	...	...
		-60		-3.5	...	...
NGC 289	182	189	3.6	4.1	9.1	11.3
		+23		+1.0	+1.7	+4.2
		-20		-0.8	-1.8	-2.7
		-55		-2.0	-4.0	-4.7
NGC 488	350	296	10.1	31.1	...	...
		+36		+7.4	...	...
		-32		-5.9	...	...
		-86		-14.3	...	...
NGC 908	200	201	7.3	7.2	...	...
		+24		+1.8	...	...
		-22		-1.5	...	...
		-59		-3.5	...	...
NGC 1087	136	141	5.9	2.8	...	...
		+17		+0.7	...	...
		-15		-0.6	...	...
		-41		-1.4	...	...
NGC 1090	170	165	7.3	5.4	16.4	23.2
		+20		+1.4	+4.4	+7.8 <sup>c</sup>
		-18		-1.1	-5.3	-4.9
		-49		-2.7	-12.5	-18.2
NGC 1241	300	250	7.9	19.2	12.4	...
		+30		+4.8	+4.4 <sup>d</sup>	...
		-27		-3.8	-5.6	...
		-73		-9.2	-12.4 <sup>d</sup>	...
NGC 1385	140	133	4.0	2.6	...	...
		+16		+0.6	...	...
		-14		-0.5	...	...
		-39		-1.2	...	...
NGC 1559	150	136	4.5	2.3	...	...
		+17		+0.6	...	...
		-15		-0.5	...	...
		-40		-1.1	...	...

TABLE 2—*Continued*

Galaxy	Observed	Baryonic Matter			Dark Matter	
	$V_{tot,max}$	$V_{b,max}$	$R(V_{b,max})$	$M_b$	$R_{10}$	$R_X$
	(km/s)	(km/s)	(kpc)	( $10^{10}M_\odot$ )	(kpc)	(kpc)
		$\Delta_{+0.1dex}$ $\Delta_{-0.1dex}$ $\Delta_{-0.3dex}$		$\Delta_{+0.1dex}$ $\Delta_{-0.1dex}$ $\Delta_{-0.3dex}$	$\Delta_{+0.1dex}$ $\Delta_{-0.1dex}$ $\Delta_{-0.3dex}$	$\Delta_{+0.1dex}$ $\Delta_{-0.1dex}$ $\Delta_{-0.3dex}$
NGC 1832	200	209	3.8	5.4	...	...
		+25		+1.4	...	...
		-23		-1.1	...	...
NGC 2090 <sup>a</sup>	160	153	1.6	1.6	...	...
		+19		+0.4	...	...
		-16		-0.3	...	...
NGC 2139	140	121	4.5	1.9	...	...
		+15		+0.5	...	...
		-13		-0.4	...	...
NGC 2280 <sup>a</sup>	210	177	6.9	6.8	8.7	...
		+5		+1.8	+1.8	...
		-19		-1.4	-3.5	...
NGC 2841	325	284	4.7	13.0	9.0	12.6
		+49		+3.3	+3.4	+5.8
		-20		-2.6	-0.6	-2.9
NGC 3198	152	120	5.6	2.3	6.8	10.5
		+14		+0.6	+3.1	+2.6
		-13		-0.5	-2.1	-2.5
NGC 3223	320	314	10.4	30.8	...	...
		+38		+7.6	...	...
		-34		-6.1	...	...
NGC 3319 <sup>b</sup>	132	50	9	0.7	2.6	3.5
		+7		+0.1	+0.7	+1.1
		-5		-0.1	-0.6	-0.8
NGC 3521	221	263	3.1	8.0	10.3	13.3
		+32		+1.9	+2.3	+4.2
		-29		-1.5	-1.8	-2.4
		-34		-3.6	-5.8 <sup>d</sup>	-6.3

TABLE 2—*Continued*

Galaxy	Observed	Baryonic Matter			Dark Matter	
	$V_{tot,max}$	$V_{b,max}$	$R(V_{b,max})$	$M_b$	$R_{10}$	$R_X$
	(km/s)	(km/s)	(kpc)	( $10^{10}M_\odot$ )	(kpc)	(kpc)
		$\Delta_{+0.1dex}$ $\Delta_{-0.1dex}$ $\Delta_{-0.3dex}$		$\Delta_{+0.1dex}$ $\Delta_{-0.1dex}$ $\Delta_{-0.3dex}$	$\Delta_{+0.1dex}$ $\Delta_{-0.1dex}$ $\Delta_{-0.3dex}$	$\Delta_{+0.1dex}$ $\Delta_{-0.1dex}$ $\Delta_{-0.3dex}$
NGC 3726	169	144	10.8	6.0	20.4	25.3
		+22		+1.5	+3.2	+3.5
		-12		-1.2	-10.6	-2.2
		-42		-2.9	-20.4 <sup>d</sup>	-16.3
NGC 3893	210	186	5.3	6.8	13.3	19.4
		+23		+1.6	+4.5	+2.6 <sup>c</sup>
		-20		-1.3	-5.5	-4.7
		-54		-3.2	-10.3	-13.4
NGC 3949	169	158	3.9	2.7	7.4	...
		+18		+0.6	+0.7 <sup>d</sup>	...
		-17		-0.5	-1.6	...
		-46		-1.2	-7.4 <sup>d</sup>	...
NGC 3953	225	227	7.7	12.0	17.8	...
		+28		+3.1	+0.3 <sup>c</sup>	...
		-25		-2.4	-4.2	...
		-66		-5.9	-14.0	...
NGC 3992	272	188	13.1	11.2	...	...
		+21		+2.8	...	...
		-21		-2.3	...	...
		-56		-5.5	...	...
NGC 4051	170	167	0.3	2.4	5.8	...
		+20		+0.6	+2.1	...
		-18		-0.5	-1.3	...
		-49		-1.1	-5.8 <sup>d</sup>	...
NGC 4062	162	110	3.4	1.1	0 <sup>d</sup>	3.9
		+14		+0.3	+1	+2.4
		-11		-0.2	0 <sup>d</sup>	-2.0
		-32		-0.6	0 <sup>d</sup>	-3.9 <sup>d</sup>
NGC 4138	195	272	1.0	4.2	7.5	17.8
		+33		+1.0	+8.9	+3.1
		-30		-0.8	-1.4	-5.8
		-79		-2.0	-7.5 <sup>d</sup>	-12.6
NGC 4651	210	173	2.6	3.7	...	...
		+32		+0.9	...	...
		-10		-0.8	...	...
		-45		-1.8	...	...

TABLE 2—*Continued*

Galaxy	Observed	Baryonic Matter			Dark Matter	
	$\overline{V}_{tot,max}$	$\overline{V}_{b,max}$	$R(\overline{V}_{b,max})$	$M_b$	$R_{10}$	$R_X$
		$\Delta_{+0.1dex}$		$\Delta_{+0.1dex}$	$\Delta_{+0.1dex}$	$\Delta_{+0.1dex}$
		$\Delta_{-0.1dex}$		$\Delta_{-0.1dex}$	$\Delta_{-0.1dex}$	$\Delta_{-0.1dex}$
		$\Delta_{-0.3dex}$		$\Delta_{-0.3dex}$	$\Delta_{-0.3dex}$	$\Delta_{-0.3dex}$
	(km/s)	(km/s)	(kpc)	( $10^{10} M_\odot$ )	(kpc)	(kpc)
NGC 4698	220	223	3.8	6.5	...	...
		+14		+1.6	...	...
		-35		-1.3	...	...
		-68		-3.2	...	...
NGC 5371	242	289	13.9	33.5	...	...
		+21		+8.5	...	...
		-43		-6.7	...	...
		-87		-16.4	...	...
NGC 5806	200	190	1.1	5.3	...	...
		+27		+1.3	...	...
		-17		-1.1	...	...
		-27		-2.6	...	...
NGC 6300	208	220	4.3	6.7	13.7	20.4
		+12		+1.7	+5.8	+2.6
		-35		-1.4	-1.3	-5.5
		-67		-3.3	-8.8	-13.5
NGC 7083	210	245	6.5	13.1	...	...
		+30		+3.3	...	...
		-27		-2.7	...	...
		-72		-6.4	...	...
NGC 7217	284	283	2.0	7.9	...	...
		+35		+2.0	...	...
		-31		-1.6	...	...
		-84		-3.9	...	...
NGC 7606	280	228	9.8	12.9	2.2	...
		+28		+3.2	+0.8 <sup>c</sup>	...
		-25		-2.6	-0.7	...
		-67		-6.2	-2.2 <sup>d</sup>	...

<sup>a</sup>Quantities are calculated from  $B - V$  instead of  $B - R$

<sup>b</sup>Quantities are calculated from  $(M/L)_{*,H}$  instead of  $(M/L)_{*,K}$

<sup>c</sup>Upper limit

<sup>d</sup>Lower limit

TABLE 3

Galaxy	original color- $M/L$			+0.1 dex			-0.1 dex			-0.3 dex		
	$c$	$V_{200}$ (km/s)	$\chi^2$	$c$	$V_{200}$ (km/s)	$\chi^2$	$c$	$V_{200}$ (km/s)	$\chi^2$	$c$	$V_{200}$ (km/s)	$\chi^2$
NGC 157	0.5	111	9.5	0.5	61 <sup>a</sup>	19.9	4.0	96 <sup>a</sup>	6.7	16.0	96	5.8
	0.5	61 <sup>a</sup>	13.8	0.5	61 <sup>a</sup>	28.2	0.5	61 <sup>a</sup>	8.2	2.0	131	7.3
NGC 289	8.0	143	0.7	6.5	148	0.8	10.5	138	0.8	11.5	138	0.8
	3.0	168	1.2	1.0	238	1.7	5.0	133	0.8	7.5	143	0.7
NGC 488	16.5	199 <sup>a</sup>	9.1	8.0	204	6.5	20.0	214 <sup>a</sup>	12.6	20.0	279	22.7
	3.0	204	5.3	0.5	199 <sup>a</sup>	6.8	8.0	199 <sup>a</sup>	5.2	18.5	199 <sup>a</sup>	6.1
NGC 908	...	...	...	...	...	...	...	...	...	20.0	116	8.7
	...	...	...	...	...	...	...	...	...	14.0	96 <sup>a</sup>	6.5
NGC 1087	...	...	...	...	...	...	...	...	...	16.5	68 <sup>a</sup>	1.3
	...	...	...	...	...	...	...	...	...	4.0	68 <sup>a</sup>	1.5
NGC 1090	1.0	400	6.4	0.5	400	9.7	5.0	160	5.3	12.0	125	4.7
	0.5	105	11.4	0.5	80 <sup>a</sup>	15.6	0.5	215	8.7	1.0	360	6.6
NGC 1241	1.5	745	4.7	0.5	150 <sup>a</sup>	9.3	3.0	745	3.4	20.0	180	3.4
	0.5	150 <sup>a</sup>	7.3	0.5	150 <sup>a</sup>	22.2	0.5	354	4.0	1.5	585	2.3
NGC 1385	...	...	...	...	...	...	...	...	...	4.0	328	0.1
	...	...	...	...	...	...	...	...	...	0.5	143	0.7
NGC 1559	...	...	...	...	...	...	...	...	...	3.5	350 <sup>a</sup>	5.1
	...	...	...	...	...	...	...	...	...	0.5	350 <sup>a</sup>	7.0
NGC 1832	0.5	89 <sup>a</sup>	8.8	...	...	...	0.5	394	4.2	20.0	94	4.0
	0.5	89 <sup>a</sup>	19.1	...	...	...	0.5	394	6.9	0.5	389 <sup>a</sup>	3.7
NGC 2090	...	...	...	...	...	...	20.0	77 <sup>a</sup>	0.8	20.0	122	1.2
	...	...	...	...	...	...	2.5	77 <sup>a</sup>	0.4	13.5	77 <sup>a</sup>	0.3
NGC 2139	2.5	301	1.5	0.5	71 <sup>a</sup>	2.2	4.0	336	1.1	7.5	261	0.8
	0.5	71 <sup>a</sup>	2.7	0.5	71 <sup>a</sup>	5.6	0.5	156	2.5	2.0	336	2.3
NGC 2280	2.0	470	1.2	1.5	475	0.5	3.0	495	0.2	5.0	375	0.2
	0.5	105 <sup>a</sup>	3.9	0.5	105 <sup>a</sup>	2.4	0.5	265	2.7	1.0	525	2.6
NGC 2841	8.5	242	13.4	3.0	402	27.6	12.5	217	11.0	15.0	207	7.0
	0.5	582	23.3	0.5	452 <sup>a</sup>	53.9	1.0	647	18.6	3.5	337	11.6
NGC 3198	6.0	140	1.7	4.0	160	2.8	8.0	130	1.1	11.5	120	0.6
	0.5	345	4.0	0.5	285	6.5	1.5	235	2.8	5.0	145	1.5
NGC 3223	0.5	733	5.3	0.5	158 <sup>a</sup>	14.8	9.5	178	5.0	20.0	178	7.1
	0.5	158 <sup>a</sup>	10.1	0.5	158 <sup>a</sup>	39.9	0.5	233	3.7	11.5	158	2.6
NGC 3319	2.0	269	0.3	1.5	314	0.3	2.5	233	0.2	3.5	189	0.2
	1.0	304	0.9	1.5	314	1.3	1.5	259	0.7	1.5	294	0.4
NGC 3521	12.5	121	3.1	7.0	136	4.3	18.5	116	2.6	20.0	121	2.2
	0.5	281	4.1	0.5	171	6.2	4.5	146	3.5	13.5	116	2.1
NGC 3726	1.0	334	1.0	0.5	379	3.6	1.0	394	0.3	6.0	154	0.6
	0.5	159	5.9	0.5	94	10.2	0.5	239	2.9	0.5	414	0.4

TABLE 3—*Continued*

Galaxy	original color- $M/L$			+0.1 dex			-0.1 dex			-0.3 dex		
	$c$	$V_{200}$ (km/s)	$\chi^2$	$c$	$V_{200}$ (km/s)	$\chi^2$	$c$	$V_{200}$ (km/s)	$\chi^2$	$c$	$V_{200}$ (km/s)	$\chi^2$
NGC 3893	4.0	159	2.3	0.5	334	4.4	18.0	94	2.2	20.0	119	4.0
	0.5	74	3.7	0.5	74 <sup>a</sup>	8.9	0.5	204	2.3	8.5	119	2.1
NGC 3949	2.0	390	2.2	0.5	365	5.5	3.0	405	0.7	7.0	245	0.03
	0.5	85 <sup>a</sup>	4.5	0.5	85 <sup>a</sup>	10.8	0.5	280	2.9	2.0	385	0.8
NGC 3953	0.5	563 <sup>a</sup>	2.0	0.5	113 <sup>a</sup>	6.5	1.5	558	0.3	9.5	183	0.02
	0.5	113 <sup>a</sup>	5.3	0.5	113 <sup>a</sup>	22.9	1.5	183	2.2	1.0	493	0.2
NGC 3992	20.0	149	0.3	14.0	154	0.3	19.5	159	0.4	20.0	164	1.2
	8.0	164	0.3	2.0	234	0.3	11.0	164	0.3	20.0	153	0.4
NGC 4051	2.0	382	1.9	1.0	322	2.9	3.0	352	1.3	10.0	152	1.0
	0.5	137	3.8	0.5	77 <sup>a</sup>	4.9	0.5	322	2.5	2.0	352	1.7
NGC 4062	18.5	97	1.7	3.5	382	1.5	20.0	102	1.7	20.0	117	2.0
	1.5	372	0.6	0.5	352 <sup>a</sup>	1.1	2.5	357	0.5	4.0	377	0.7
NGC 4138	1.0	375 <sup>a</sup>	15.7	0.5	295	30.1	8.5	115	9.9	20.0	105	7.3
	0.5	75 <sup>a</sup>	23.6	0.5	75 <sup>a</sup>	43.0	0.5	75 <sup>a</sup>	15.4	1.0	375	10.8
NGC 4651	3.0	517	2.3	1.0	557 <sup>a</sup>	4.9	15.0	142	2.0	20.0	152	3.0
	0.5	112 <sup>a</sup>	6.1	0.5	112 <sup>a</sup>	11.1	1.0	307	5.8	3.5	382	5.7
NGC 4698	...	...	...	...	...	...	...	...	...	3.5	525	19.2
	...	...	...	...	...	...	...	...	...	0.5	105 <sup>a</sup>	29.2
NGC 5371	...	...	...	...	...	...	0.5	217	6.2	9.0	137	0.9
	...	...	...	...	...	...	0.5	107 <sup>a</sup>	15.1	0.5	197	0.8
NGC 5806	...	...	...	...	...	...	14.0	96 <sup>a</sup>	1.6	20.0	96 <sup>a</sup>	3.7
	...	...	...	...	...	...	1.0	101	0.7	6.0	96 <sup>a</sup>	1.2
NGC 6300	...	...	...	...	...	...	5.0	174	9.5	20.0	109	9.3
	...	...	...	...	...	...	0.5	209 <sup>a</sup>	7.0	8.0	119 <sup>a</sup>	4.6
NGC 7083	...	...	...	...	...	...	...	...	...	13.0	126	1.1
	...	...	...	...	...	...	...	...	...	0.5	361	0.9
NGC 7217	...	...	...	...	...	...	...	...	...	20.0	176	15.6
	...	...	...	...	...	...	...	...	...	19.0	106 <sup>a</sup>	4.0
NGC 7606	17.5	142 <sup>a</sup>	1.7	9.5	142 <sup>a</sup>	2.5	20.0	157	1.4	20.0	192	2.0
	0.5	447	3.0	0.5	142 <sup>a</sup>	3.6	2.5	357	2.7	12.0	187	2.3

<sup>a</sup> Limit of parameters searched.

NOTE.—The first and second rows for each galaxy list information for the uncontracted and contracted halo models.

TABLE 4

Galaxy Property	Correlation Coefficients			
	All Data		Without Outliers <sup>a</sup>	
	$R_X/h_{IR}$	$R_X$	$R_X/h_{IR}$	$R_X$
$V_{tot,max}$	0.41	...	0.90	...
$V_{b,max}$	0.85	...	0.96	...
$R(V_{b,max})$	...	0.22	...	0.58 <sup>b</sup>
T-type	0.89	...	0.90	...
$\log_{10}M_b$	0.65	...	0.90	...
$h_{IR}$	...	0.21	...	0.80 <sup>c</sup>
$R_{10}$	...	0.94	...	0.98
$B$	0.36	...	0.77	...
$K^d$	0.41	...	0.80	...
$\mu_{o,B}$	0.51	...	0.68	...
$\mu_{o,K}$	0.64	...	0.87	...

<sup>a</sup>Outliers are NGC 2841 and NGC 4138.

<sup>b</sup>Outliers for this relation are NGC 3319 and NGC 4062.

<sup>c</sup>NGC 3319 is not included because it is an outlier in this relation.

<sup>d</sup>NGC 3319 is not included because it does not have  $K$ -band surface brightness profiles with high enough signal-to-noise to derive an integrated magnitude.